Supplementary Material

An alternative plant-like cyanobacterial ferredoxin with unprecedented structural and functional properties

Taiki Motomura[§‖], Lidia Zuccarello[§+±], Pierre Sétif[#], Alain Boussac[#], Umena Yasufumi[‖], David Lemaire[+], Jatindra N.Tripathy†, Miwa Sugiura[‡], Rainer Hienerwadel[±]*, Jian-Ren Shen [‖]*, Catherine Berthomieu[+]*.

Supplementary Figure 1: ESI-MS data of purified Fd1 and Fd2 from *T. elongatus*.

A) ESI-MS spectrum of Fd1 in the denaturing mode

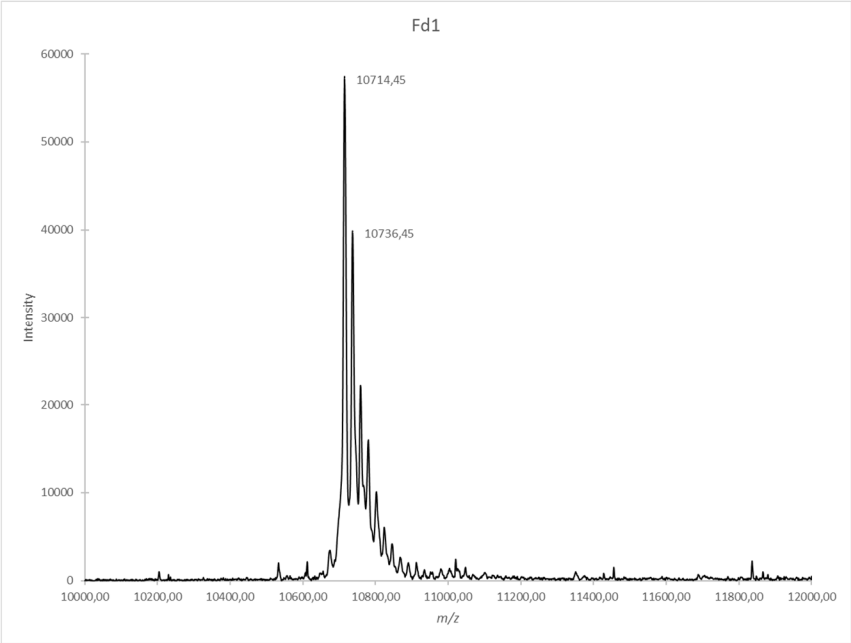

B) ESI-MS spectrum of Fd2 in the denaturating mode

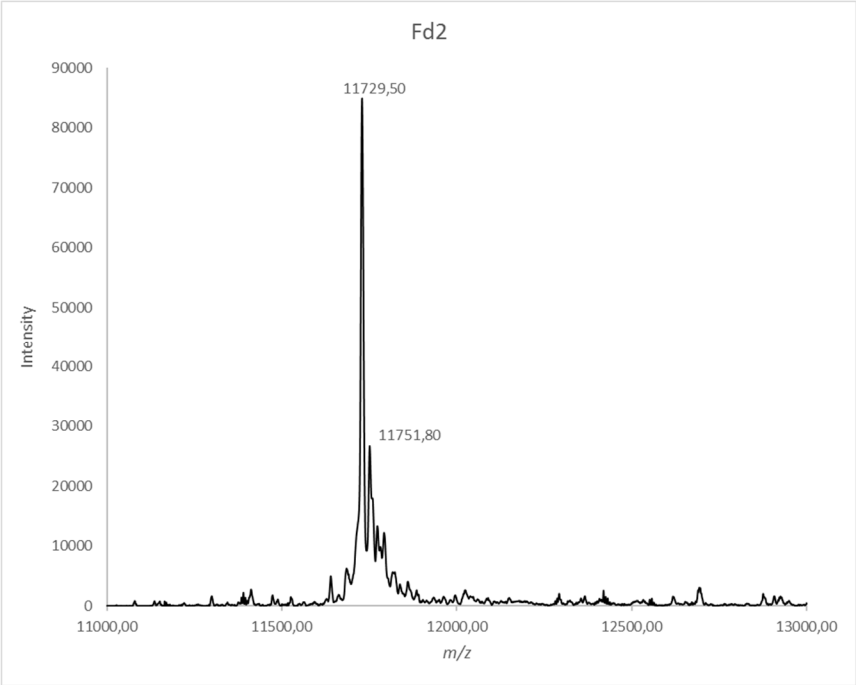

C) ESI-MS spectrum of Fd1 in the native mode

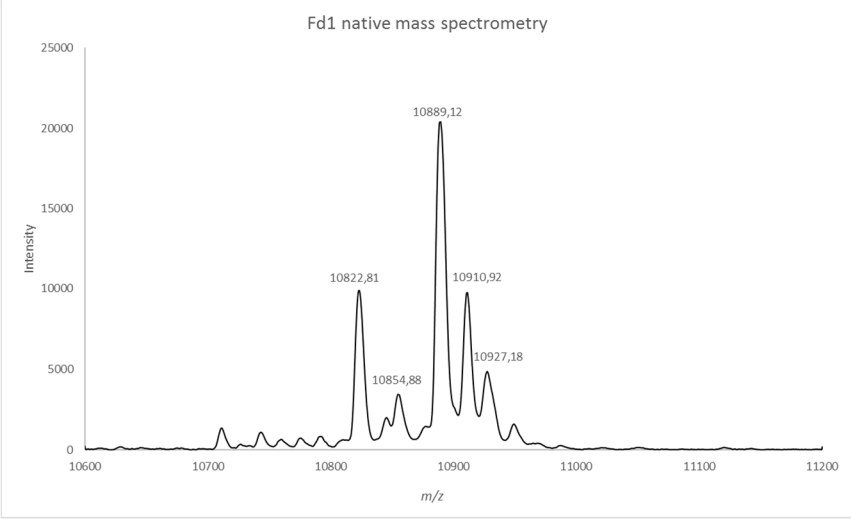

The main peak (*m/z* = 10889.12 Da) corresponds to the experimental mass for native Fd1. Indeed, the theoretical mass of the protein with the [2Fe-2S] cluster (calculated mass of 176 Da) and without four Cys thiol protons is 10887.8 Da. A *circa* +23 Da Na-adduct was observed at 10910.92 and a +38 Da K-adduct was observed at 10927.18 Da. The peak at 10822.81 Da probably corresponds to the protein with two Fe attached to it, but without the

bridging sulfurs. The detection of such a peak suggests that a fraction of the proteins has lost the two bridging sulfurs of the [2Fe-2S] cluster in the conditions used to record the ESI-MS spectra.

D) ESI-MS spectrum of Fd1' in the native mode

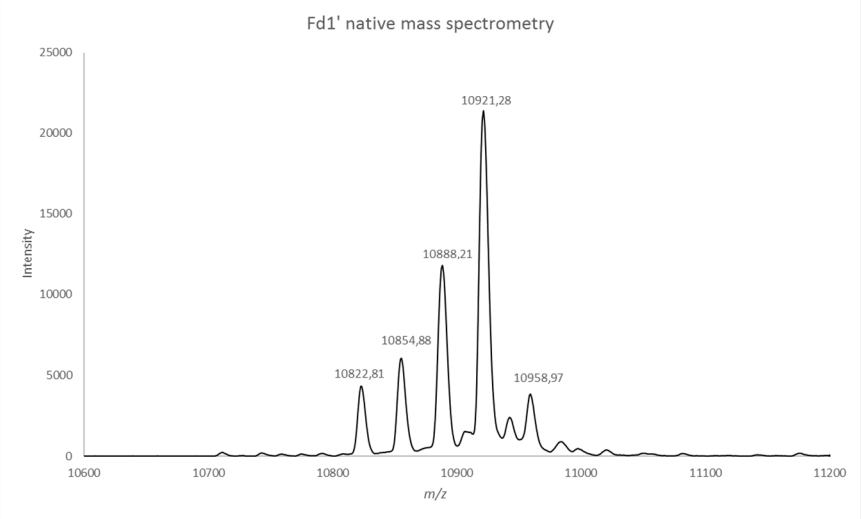

The main peak at 10921,28 Da corresponds to the mass of native Fd1 with the [2Fe-2S] cluster bound (*i.e. m/z* = 10889.12 Da) and with a mass adduct of circa + 32 Da. We also observe the peak at *m/z* = 10888,21 Da which corresponds to a fraction of native Fd1.

E) ESI-MS spectrum obtained with Fd1' in denaturating mode, after exchange in acetate buffer

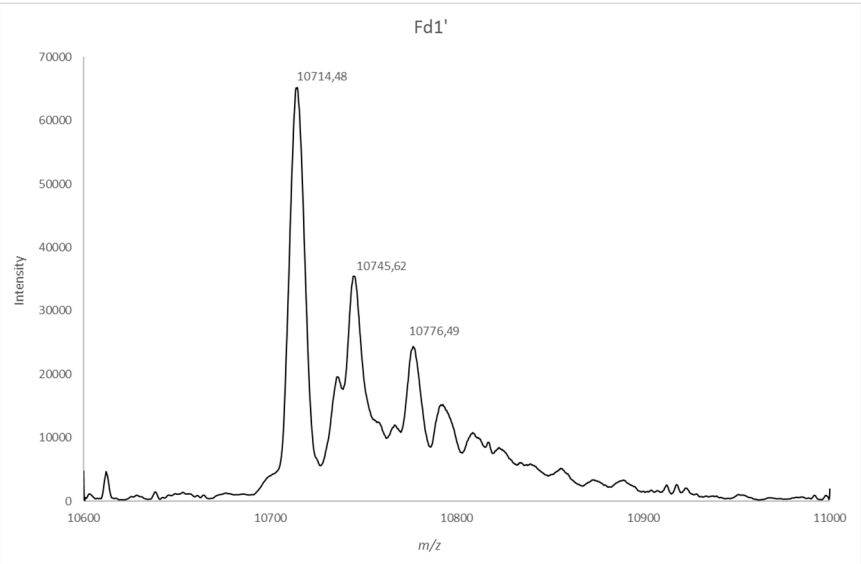

The larger peak at *m/z* = 10714,48 Da corresponds to the theoretical mass of Fd1. Another large peak is observed at *m/z* = 10745,62 Da, which corresponds to an adduct of *circa* 32 Da. Another adduct is observed at *m/z* = 10776,49 Da (*circa* + 62 Da).

Supplementary Figure 2: Redox midpoint potentials of Fd1, Fd2, Fd1' and FdN

The determination of the midpoint potentials of Fd1, Fd1', Fd2 and FdN was done by spectro-electrochemical titrations in the UV-Vis range.

A- Superposition of the titrations in the oxidative mode for Fd1 (orange), Fd1' (black), Fd2 (green) and FdN (blue) at pH 7.5. The experimental data were fitted by a Nernst equation with n=1. E_m values given in Table 2 are an average of data obtained in oxidation and reduction mode.

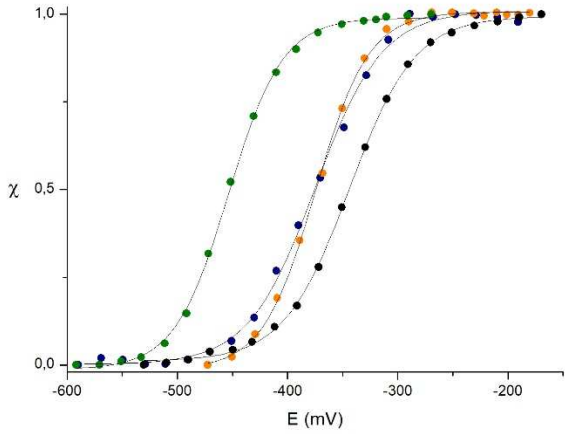

B – Superposition of the titrations in the reductive mode for Fd1 (orange), Fd1' (black), Fd2 (green) and FdN (blue) at pH 7.5.

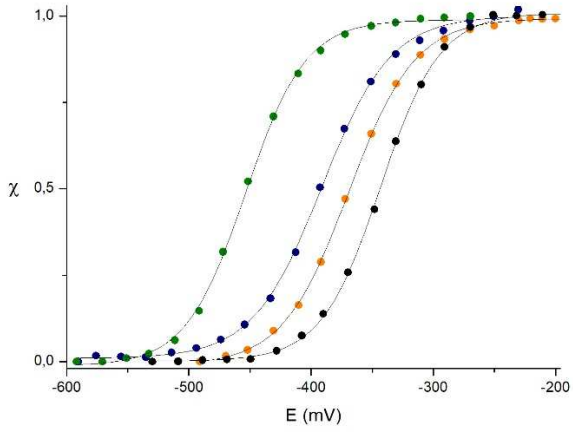

C - Superposition of titrations in the reductive (red) and in the oxidative (blue) mode for FdN, Fd1, Fd1’ and Fd2 at pH 7.5.

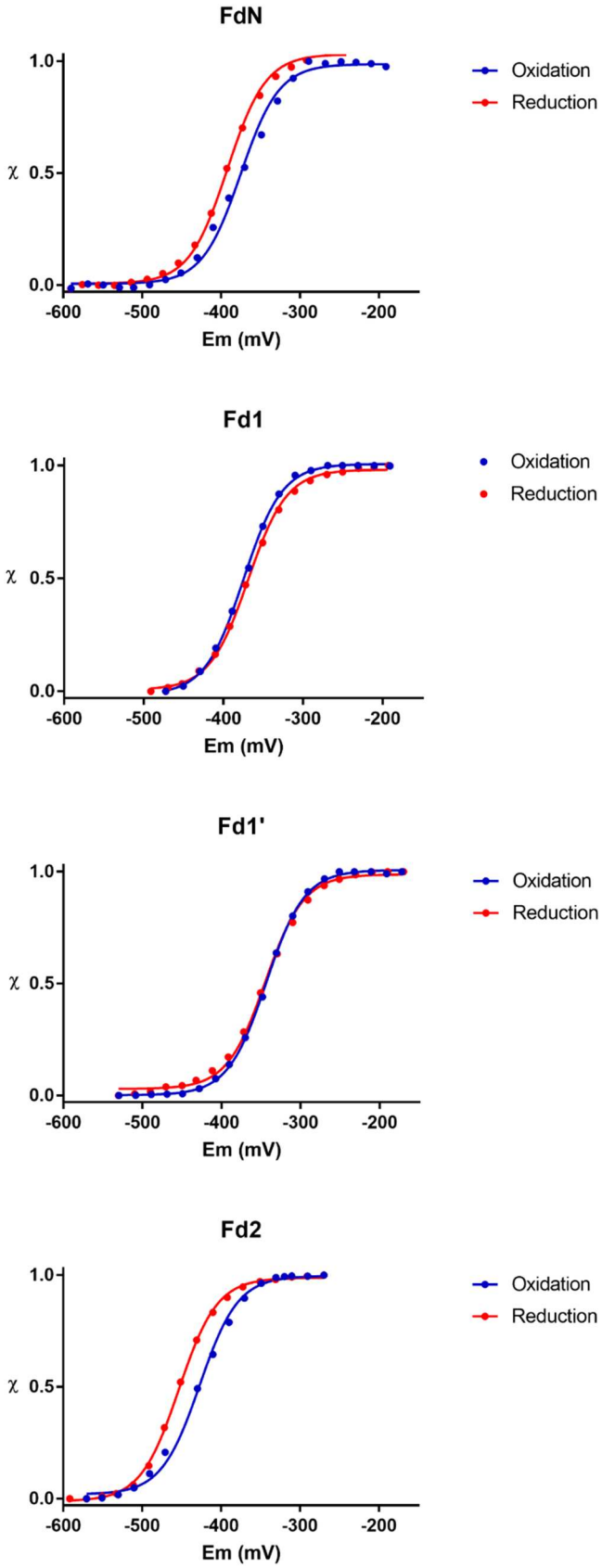

D - Effect of pH on the midpoint potential of Fd1: Electrochemical titration of Fd1, pH 7,5 (blue) and pH 10 (green).

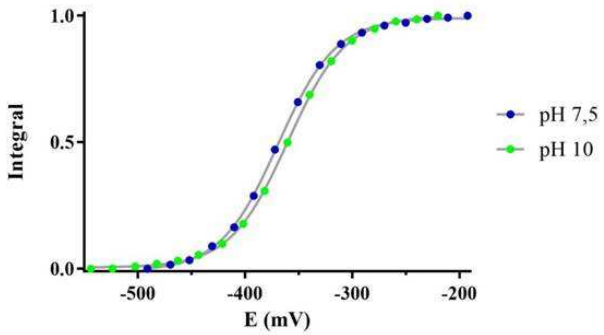

E) - Summary of the midpoint potentials and R^2 values resulting from the fit of experimental data using a Nernst curve with n fixed to 1.

		Fd2	**Fd1**	**FdN**	**Fd1'**
Oxidation	**Em**	-427	-375	-375	-343
	R^2	0.9976	0.9996	0.9958	0.9997
Reduction	**Em**	-453	-369	-392	-344
	R^2	0.9996	0.9993	0.9986	0.9983

Supplementary Figure 3: Crystals of Fd2 from *T. elongatus***.**

A plate-shaped crystal with a brown color was grown from urchin-like crystal by the sitting drop vapor diffusion method. The bar represents 50 µm.

Supplementary Figure 4: FoFc map near residues Val65, Asp66, Ser68, Asp69 and His70, Val83, Cys94 and Ser97.

Green: positive, red: negative.

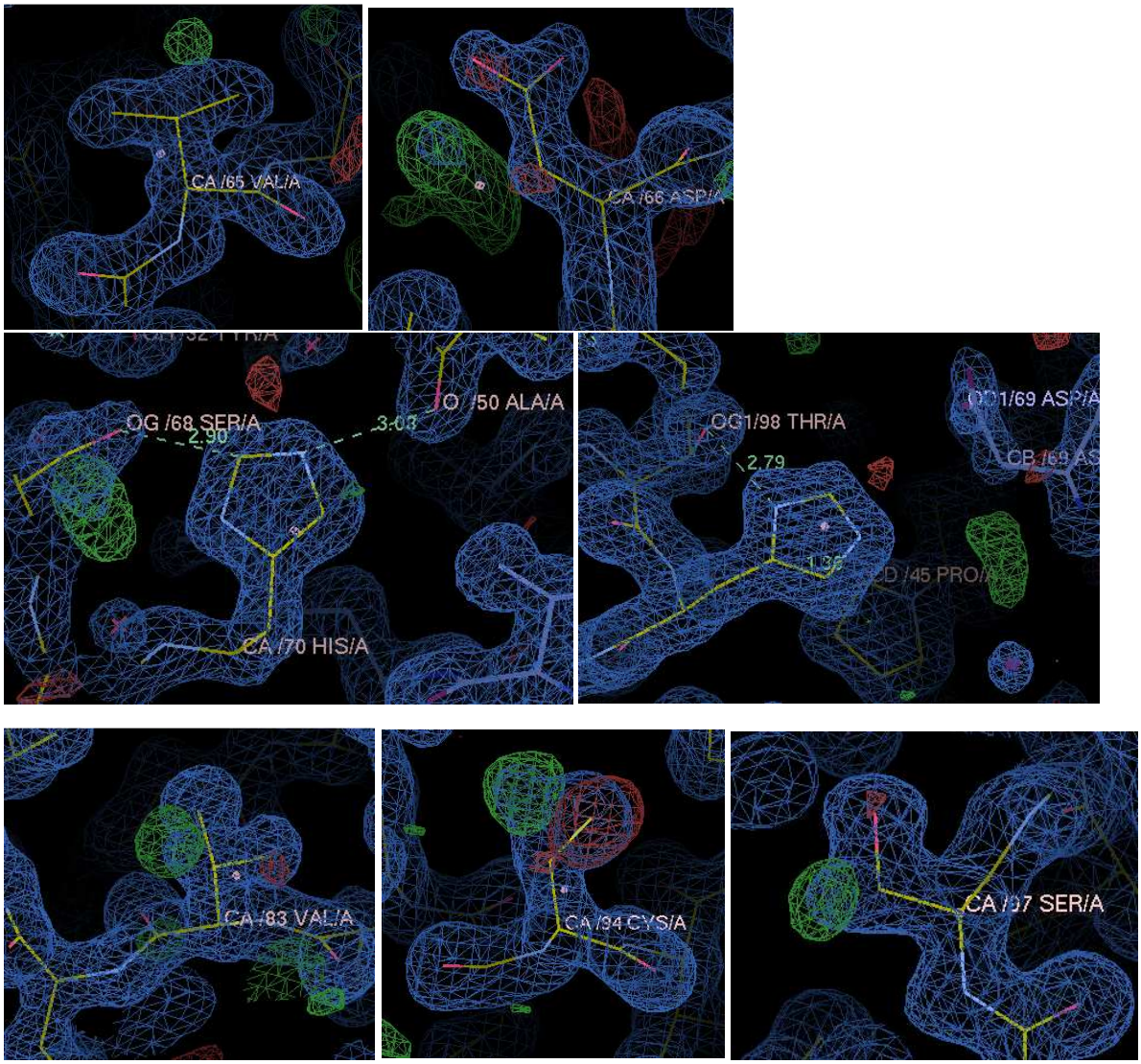

Supplementary Figure 5: Comparison of RMSDs between the Cα of Fd1, Fd2 and FdN.

The distance differences between the Cα atoms of three Fds were calculated based on secondary structure matching, using lsqkab [1]. Distance differences between **(A)** Fd1 (PDB ID: 5AUI, [2]) and Fd2 (present study), **(B)** Fd1 and FdN (PDB ID: 1fxa, [3], A monomer), **(C)** Fd2 and FdN. The overall RMSDs are given at the bottom of each figure and are represented as a horizontal orange line in each figure panel.

A)

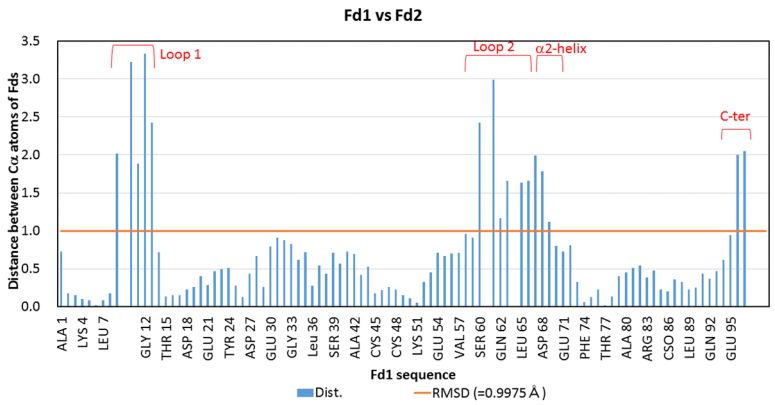

B)

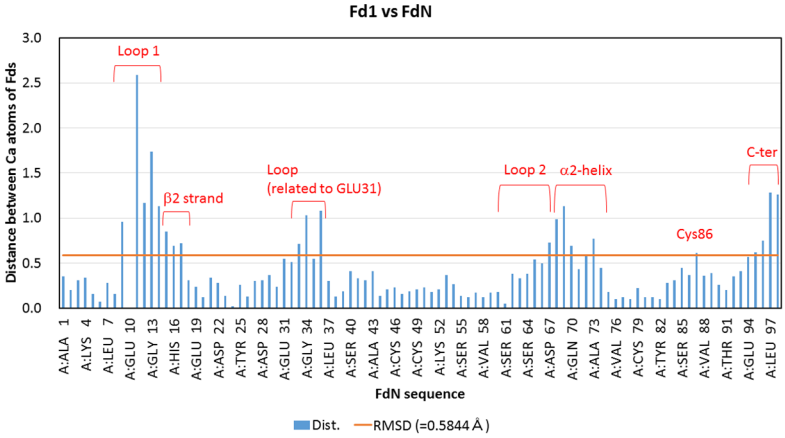

C)

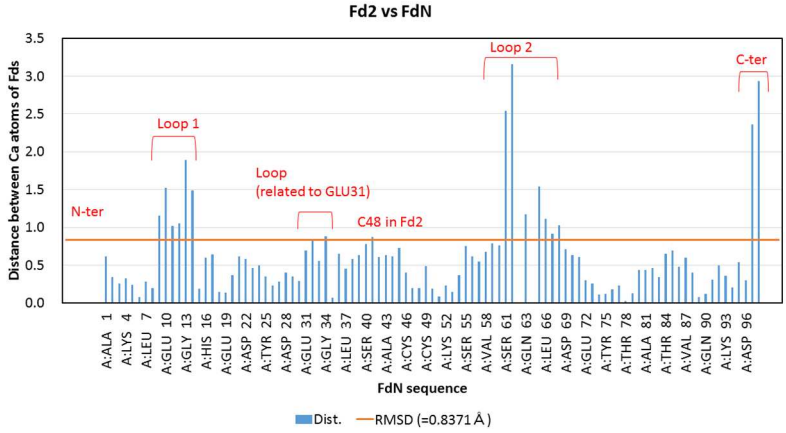

Supplementary Figure 6: Comparison of the Loop 1 structure in Fd1 and Fd2.

The structures of loop 1 of Fd2 **(A)** and Fd1 (PDBID: 5aui [2]) **(B)** are shown. The dashed lines indicate hydrogen bonds between the residues. The bond lengths are as follows: **(A)** A16-R19, 2.91 Å; N16-G20, 2.94 Å; N16-L21, 2.97 Å; N16-T98, 2.98 Å; **(B)** R10-S14, 2.84 Å; R10-T91, 2.76 Å; R10-N92, 2.90 Å; P11-G13, 2.84 Å; D12-S14, 3.06 Å. **C)** Superimposition of the loop 1 structures of Fd1 and Fd2.

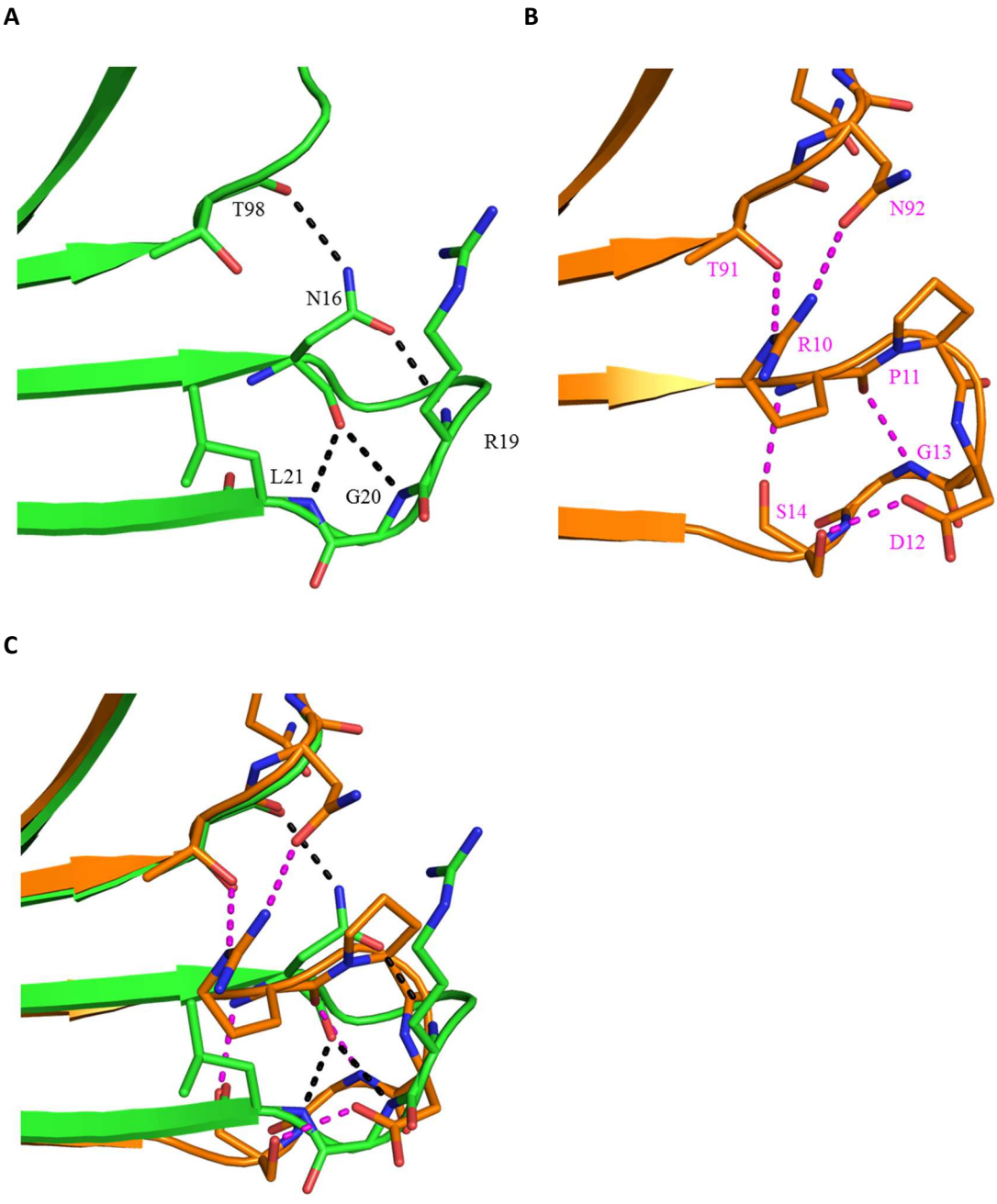

Supplementary Figure 7: Comparison of the Loop 2 structure in Fd1 and Fd2**.**

The structures of loop 2 in Fd2 **(A)** and Fd1 (PDBID: 5aui [2]) **(B)** are shown. The dashed lines indicate hydrogen bonds between the residues. The bond lengths are as follows: **(A)** T64-C94, 3.04 Å; D66-R4, 2.77Å; Q67-L84, 2.81 Å; S68-H70, 2.70 Å and 2.84 Å; S68-S71, 3.02 Å; S68-A87, 2.83 Å; F72-G51, 2.74 Å; K74-K77, 2.76 Å (peptide N-side chain O) and 2.86 Å (side chain N- side chain O), K76-A108, 2.68 Å; **(B)** E57-CSO87, 2.79 Å (peptide N-side chain O) and 2.94 Å (peptide O-side chain O); Q60-Q63, 2.87 Å; Q60-L77, 2.95Å; D62-Y25, 3.05 Å; Q63-F65, 2.96 Å; Q63-L66, 2.75 Å; S64-G44, 2.79 Å; D67-Q70, 2.88 Å (side chain O-peptide N) and 2.98 Å (peptide N-side chain O). **(C)** Superimposition of loop 2.

A

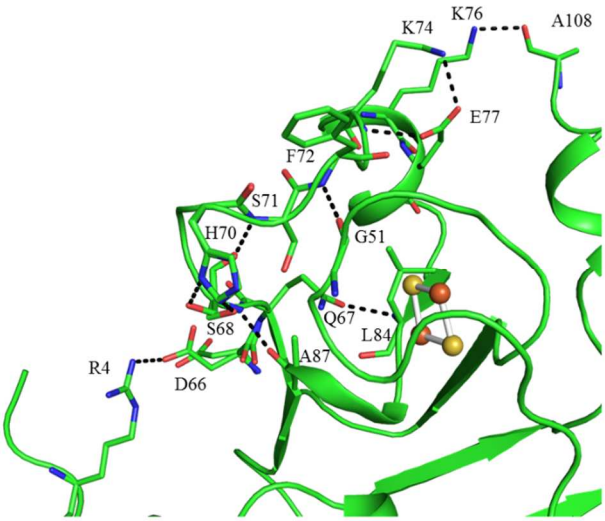

B

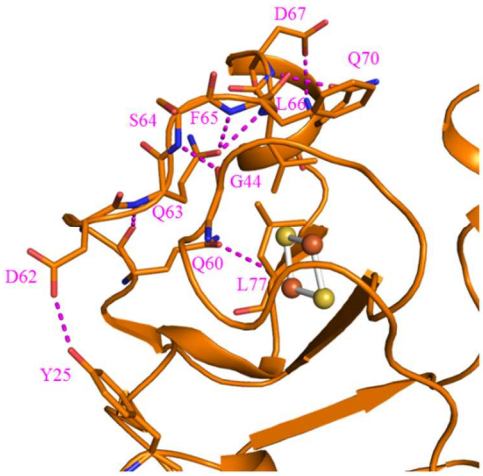

C

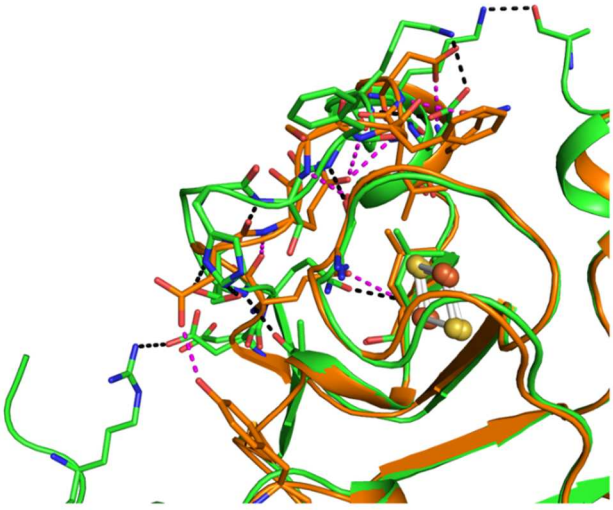

Supplementary Figure 8: Effect of $^{1}H_2O/^{2}H_2O$ exchange on the reduced-*minus*-oxidized FTIR difference spectra recorded with Fd1 and Fd2.

A) Effect of $^{1}H_2O/^{2}H_2O$ exchange in the mid infrared for Fd1 (top) and Fd2 (bottom)

Spectra in H_2O are in orange for Fd1 and in green for Fd2. The corresponding spectra recorded in $^{2}H_2O$ are in dark grey. The inset presents the absorption region of ν(S-^{2}H) modes in the reduced-minus-oxidized FTIR difference spectrum recorded with Fd1 in $^{2}H_2O$.

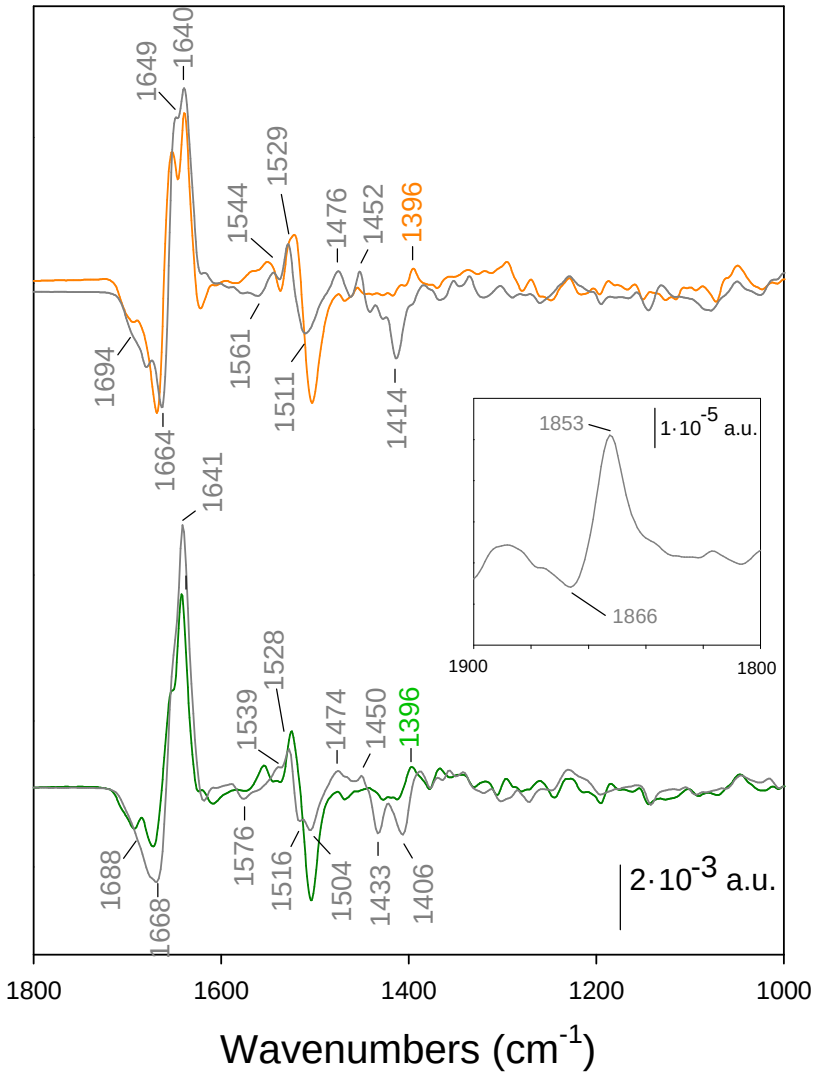

Down shifts by less than 10 cm^{-1} are expected upon $^{1}H_2O/^{2}H_2O$ exchange for amide ν(C=O) modes, *i.e.* up to 10 cm^{-1} for α-helix and less than 5 cm^{-1} for β-sheet secondary structures [4, 5]. The band frequencies at 1694 and 1639 cm^{-1} are not sensitive to $H_2O/^{2}H_2O$ exchange while the bands at 1668 and 1652 cm^{-1} are downshifted by -4 and -3 cm^{-1}, respectively. This supports the assignment to peptide carbonyl groups from random coil and/or α helix at 1668 and 1653

cm^{-1}, to carbonyl groups involved in β-sheet structures at 1640 cm^{-1}, or to carbonyl groups free of hydrogen bonding interactions above 1680 cm^{-1}. For Fd1, an additional band observed at 1680 cm^{-1} in ^2H_2O for oxidized Fd1 shows that at least two different groups contribute to the broad band at *circa* 1700-1694 cm^{-1} in H_2O. The behavior upon $^1H_2O/^2H_2O$ exchange in the 1800-1620 cm^{-1} region is similar for Fd2. This suggests a dominating contribution of Amide I bands. They appear almost at the same frequencies for Fd2 and Fd1, with a slightly higher frequency of the ν(C=O) mode at 1642 cm^{-1} (1641 cm^{-1} in ^2H_2O), and at 1672 cm^{-1} (*vs* 1668 cm^{-1} in Fd1) and with different relative band intensities.

Amide II modes are expected to largely downshift in ^2H_2O. They are identified in ^1H_2O at 1503 cm^{-1} and at 1551 and 1522 cm^{-1} for $Fd1_{ox}$ and $Fd1_{red}$, respectively, by their large downshift to 1413 cm^{-1} (-88) and 1476 (-75) and 1452 cm^{-1} (-70) in ^2H_2O. For $Fd2_{ox}$, in contrast to Fd1, two bands are identified at 1433 and 1406 cm^{-1} in ^2H_2O, which should result from the downshift of the Amide II mode at 1503 cm^{-1}. They suggest different properties of the Amide II modes sensitive to the [2Fe-2S] cluster reduction as compared to Fd1.

In the spectrum recorded in ^2H_2O, bands at 1561 and 1511 cm^{-1} for $Fd1_{ox}$ and at 1576, 1516 and 1504 cm^{-1} for $Fd2_{ox}$ cannot result from Amide II modes with deuterated N^2H. These bands result either from Amide II modes where the NH has not been exchanged in N^2H or from contributions of amino acid side chains. Bands at 1516-1504 cm^{-1} are typical for a tyrosine ν_{19}(CC) side chain mode [6, 7]. This mode is expected to shift by a maximum of -3 cm^{-1} upon $^1H/^2H$ exchange. These modes could be superimposed to contributions from Amide II modes in H_2O. The FTIR data thus suggest that a tyrosine side-chain contributes to the redox-induced structural changes in both Fd1 and Fd2. The bands at 1561 and 1576 cm^{-1} are in the range where carboxylate $\nu_{as}(COO^-)$ modes of aspartate or glutamate contribute [6]. These modes are expected either at the same frequency or upshifted by a few wavenumbers in ^2H_2O. For $Fd1_{red}$ and $Fd2_{red}$, bands at 1544 and 1539 cm^{-1} could correspond to these modes, and the low frequency would indicate a strong interaction with a positively charged group. The positive band at 1396 cm^{-1} in the spectra recorded with all Fds is tentatively assigned to the corresponding $\nu_s(COO^-)$ mode of a glutamate or aspartate residue. The latter mode is less sensitive to changes in hydrogen bonding interactions. Finally, the band at 1622 cm^{-1} for $Fd1_{ox}$, which disappears or is largely downshifted in ^2H_2O could correspond to a lysine or arginine side-chain mode. This band seems downshifted to 1608 cm^{-1} in $Fd2_{ox}$.

Finally the bands at 1866/1853 cm^{-1} in the figure inset recorded with Fd1 and not with Fd2 or FdN are typical for a cysteine ν(S-^{2}H) mode [8]. It corresponds to the ν(S-H) mode observed

at 2567/2548 cm^{-1} of Fd1 in H_2O, assigned to a cysteine side chain, which is sensitive to the change in redox state of the [2Fe-2S] cluster.

B) Effect of $^1H_2O/^2H_2O$ exchange on the 1400-1000 cm^{-1} region.

Reduced-*minus*-oxidized FTIR difference spectra recorded with FdN (blue line), Fd1 (orange line), Fd1' (black line) and Fd2 (green line) in the region between 1400 and 1000 cm^{-1} in H_2O. For Fd1 and Fd2, spectra recorded in ^2H_2O are shown with grey lines.

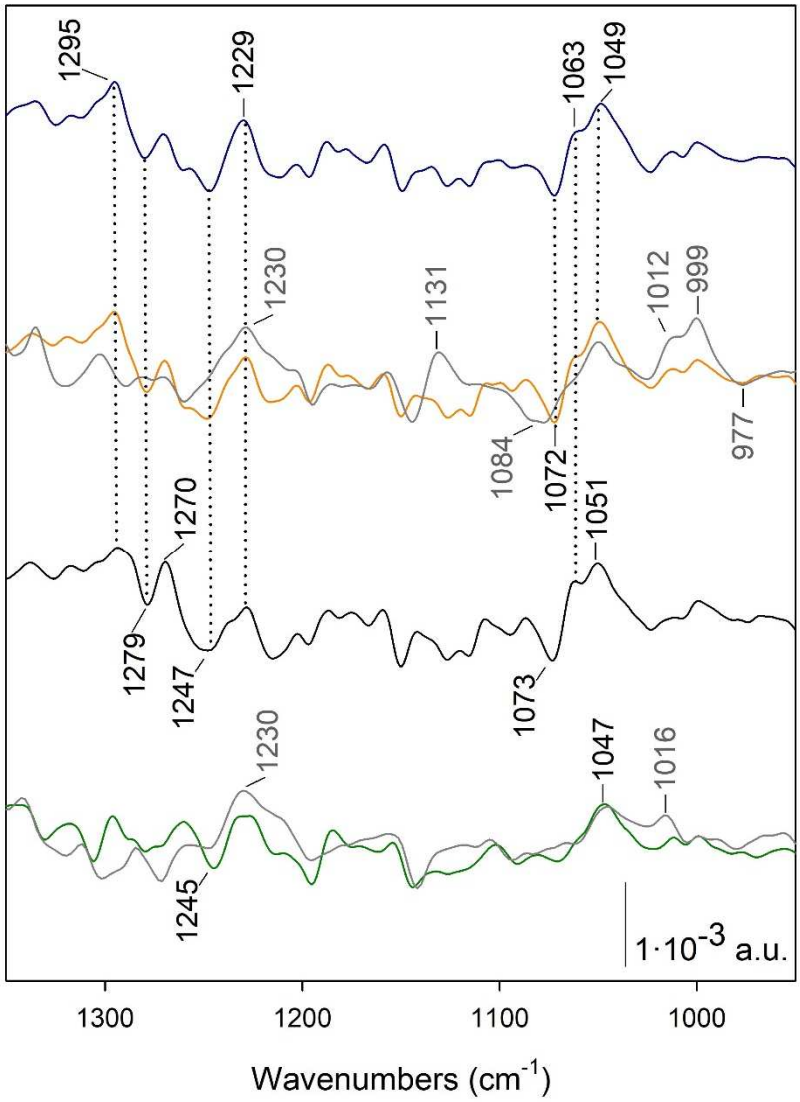

Two IR modes from threonine and serine side chains are expected in the 1300-900 cm^{-1} region: the δ(COH) bending mode, which is largely downshifted upon deuteration, and the ν(CO) mode, only slightly shifted in ^2H_2O ([9] and references therein). In the region where δ(COH) modes are expected to contribute, bands observed at 1295(+) cm^{-1}, 1279(-) cm^{-1}, and 1247(-)

cm^{-1} in the spectra recorded with Fd1, FdN and Fd1' seem absent or largely shifted in ^2H_2O. The bands at 1295/1279 cm^{-1} are also absent in the spectrum recorded with Fd2, while the band at 1247 cm^{-1} is conserved in Fd2. Bands at 1072(-) cm^{-1}, 1063(+) cm^{-1} and 1049(+) cm^{-1} observed in the spectra recorded with Fd1, FdN and Fd1' are still present and only slightly modified in the spectrum recorded in ^2H_2O. The bands at 1073/1063 cm^{-1} are absent in the spectrum recorded with Fd2.

We thus assign the bands at 1295(+)/1279(-) cm^{-1} to the δ(COH) bending mode of either threonine or serine and propose that they are shifted to 999(+)/977(-) cm^{-1} in ^2H_2O, in the spectrum recorded with Fd1, in agreement with literature data. The bands at 1072(-)/1063(+) cm^{-1} are tentatively assigned to corresponding ν(CO) mode. Since the difference bands at 1295(+)/1279(-) cm^{-1} and 1072(-)/1063(+) cm^{-1} are absent in the reduced-minus-oxidised spectrum of Fd2, (as well as the difference band at 999(+)/977(-) cm^{-1} in the spectrum recorded in ^2H_2O), they are tentatively assigned to the CysSerThrCys motif, present in Fd1 and FdN and replaced by the CysValAsnCys motif in Fd2. The structural change at the level of the Ser47 described for FdN reduction could explain the changes in the IR mode frequencies of Ser 47 or Thr48 side chains upon Fd reduction.

Supplementary Figure 9: Hydrogen bonding interactions of the fifth CysSγ in Fd1 and Fd2 structures.

The environment around the fifth Cys is compared for Fd2 (green), Fd1 (in orange transparent for PDB ID: 5aui [2], and in pink for the new Fd1 structure), and FdN (in blue PDB ID: 1fxa [3]). The hydrogen bonds are shown in dashed lines in black for Fd2 and red for Fd1 (new structure). Both Cys-Sγ can form hydrogen bonding interactions: Cys87Sγ in Fd1 (new Fd1 structure) with the peptide carbonyl oxygen of Glu57 at 3.14 Å, and for Cys94Sγ in Fd2 with the peptide carbonyl oxygen of Thr64 at 3.05 Å.

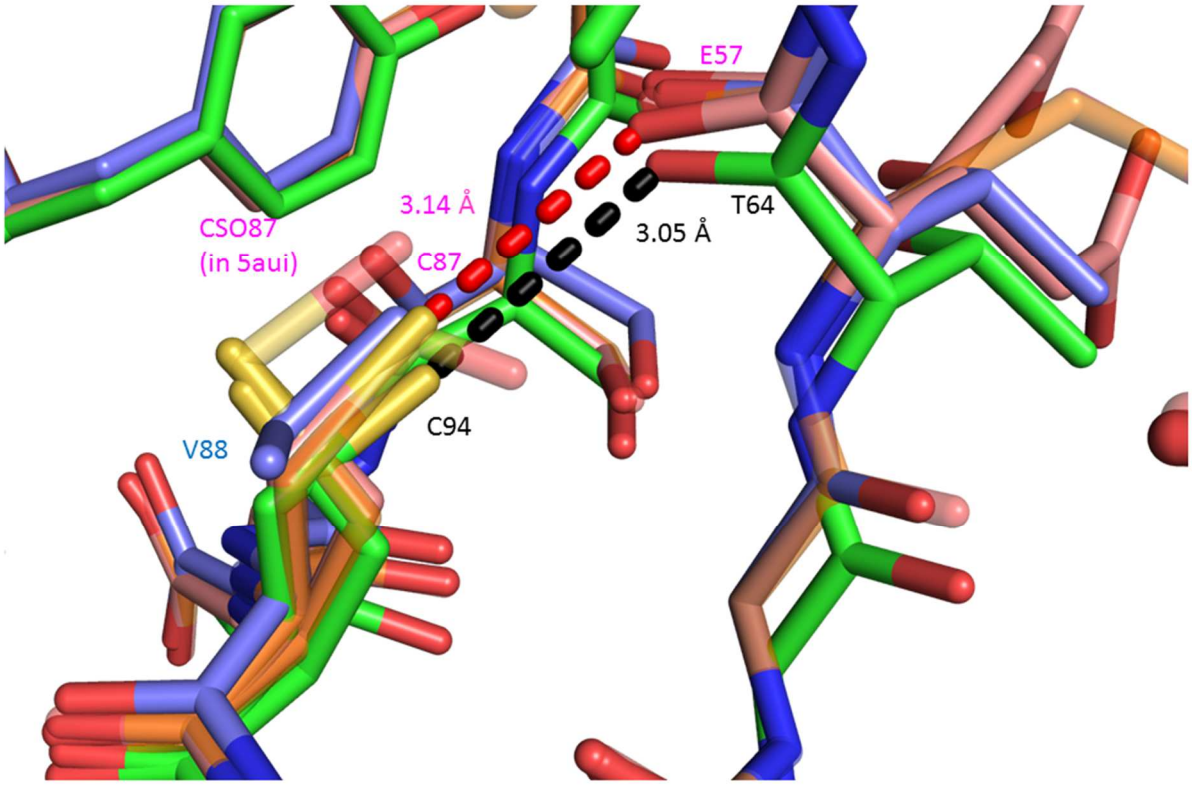

Supplementary Figure 10: Orientation of the arginine and serine residues. Consequences on Cys46 environment

The environment around Arg42 **(A)** and Cys46, Ser40 and Thr48 (Fd1 numbering) **(B)** is compared for Fd2 (transparent green) and Fd1 (orange for PDB ID: 5aui [2] and pink for the new Fd1 structure) as well as for FdN (in blue, PDB ID: 1fxa , [3]). The hydrogen bonds are shown with dashed lines in black for Fd2, magenta for Fd1 PDB ID: 5aui, red for the new Fd1 structure and in blue for FdN.

A

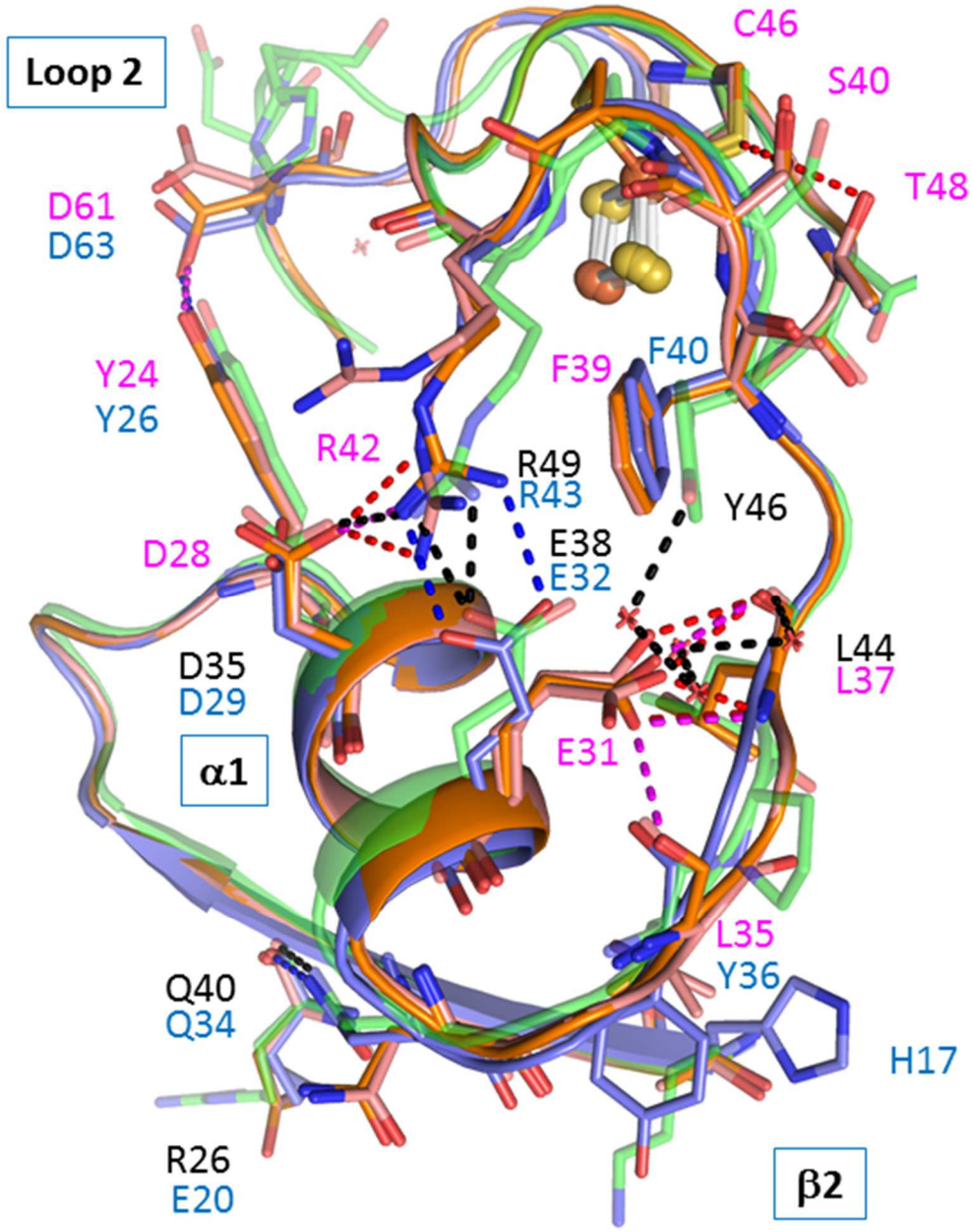

B

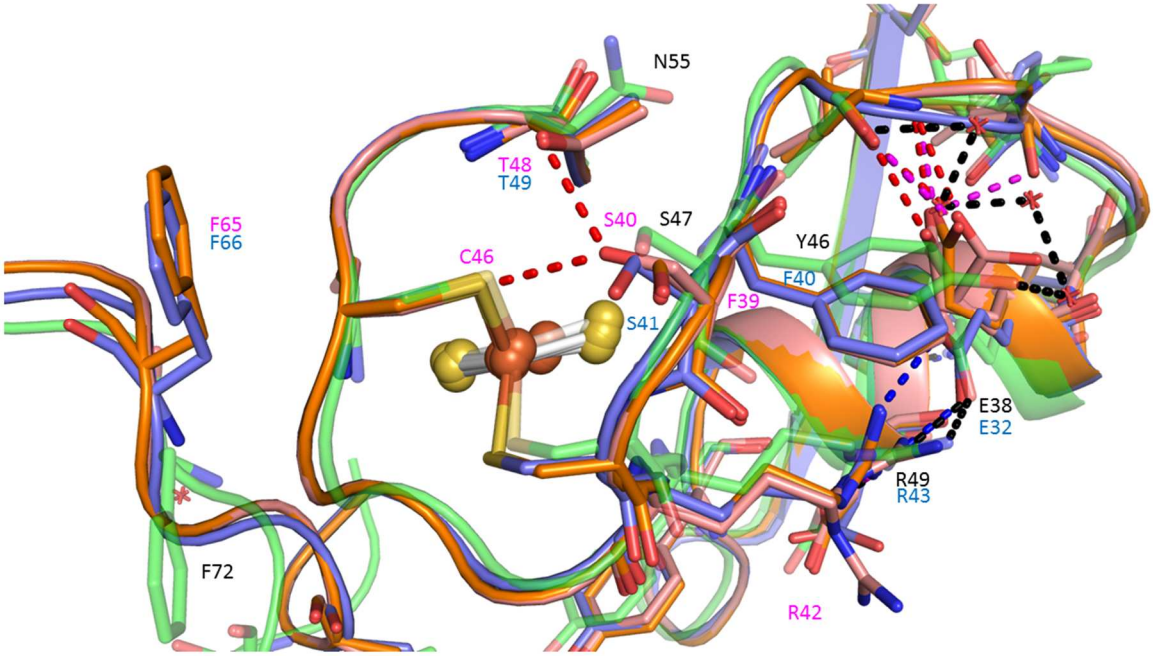
N55
T48
T49
S40
S47
F65
F66
C46
Y46
F40
F39
S41
E38
E32
R49
R43
F72
R42

Supplementary Figure 11: Crystal structure of a major ferredoxin, Fd1 coded by *tlr1009* in *T. elongatus*.

(A) Ribbon model of the whole structure. The crystal structure contains residues 2-98 (the full length of the protein is 98 residues), a [2Fe-2S] type iron-sulfur cluster (shown in ball), and a tentatively assigned sulfate ion and two benzamidines (shown in sticks). The color of the Fd1 structure is in cyan, iron atoms are in brown, sulfur and oxygen atoms of the sulfate iron are shown in yellow and red, and the benzamidines are shown in gray.

(B) Superposition of the Fd1 structure determined in the present study with that reported previously (PDB ID: 5aui [2], protein body, orange ; benzamidine, blue). The structures of the two Fd1 were superposed by the SSM protocol in Coot [10]. Residues having remarkable difference structures are shown in sticks. In the new structure (PDB ID :6jo2), Ser40 has two conformations, one with its side chain facing the iron cluster with 0.33 occupancy, and the other one facing Asp36 from the adjacent molecule with 0.67 occupancy. The main-chains of Leu35 and Asp36 were flipped, which may be caused by crystal packing because Ser40 was close to the Leu35 and the Asp36 residues, as well as Glu31 of the adjacent molecule in the crystal. Arg42 has also two conformations in the new structure, and no remarkable environmental differences were found near Arg42. The 87th residue in the new structure is cysteine, in agreement with the amino acid sequence but not S-hydroxycysteine that was reported in the previous structure (PDB ID : 5aui).

A B

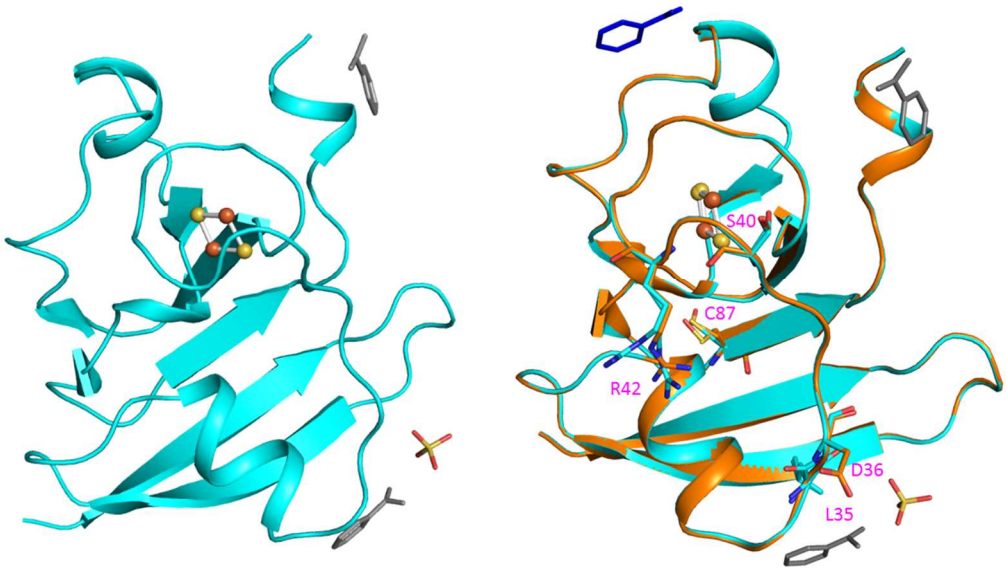

Supplementary Figure 12: Kinetics of Fd2 reduction by PSI.

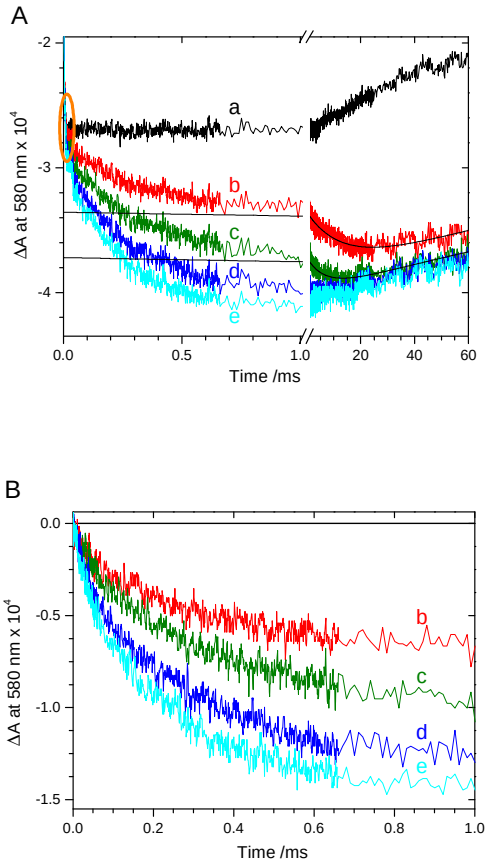

Flash-induced absorption measurements were performed at 580 nm with increasing Fd2 concentrations (0, 1.00, 2.02, 4.01, 7.93 µM from a to e) and with [PSI] decreasing from 0.218 to 0.206 µM along with Fd2 addition (or buffer in the reference cuvette). Best-fits were performed with real PSI concentrations but data in the figure were normalized to 0.218 µM PSI for easier comparison. **Part A** displays raw kinetics. Both P700 oxidation and (F_A F_B) reduction give rise to an initial fast bleaching (negative absorption signal) whereas Fd reduction by (F_A F_B)$_{1red}$ gives rise to a further bleaching with kinetics depending upon the Fd concentration (traces b to e). In trace a (no Fd), the slow signal decay is due to a recombination reaction between $P700^+$ and (F_A F_B)$_{1red}$. In the presence of Fd, the fastest component of the decay kinetics (up to *c*. 0.5 ms after the flash) is first-order with its rate being constant (not [Fd]-dependent) and its amplitude increasing with [Fd]. It is attributed to intracomplex ET from (F_A F_B)$_{1red}$ to Fd within PSI:Fd complexes which are preformed before flash excitation. It is followed by a second-order component with its rate being [Fd]-dependent and its amplitude decreasing with [Fd]. This component is clearly observed in traces b and c whereas its amplitude is much smaller

in traces d and e. It is attributed to Fd reduction by the part of PSI which does not bind Fd before flash excitation and where diffusion-limited binding of Fd to PSI-$(F_A\ F_B)_{1red}$ precedes Fd reduction itself and limits the rate of this reduction. After completion of Fd reduction (*i.e.* after ≈30 ms for b, 15 ms for c and less than 10 ms for d and e), the slow decay is attributed to $P700^+$ reduction by the exogenous electron donor $DCPIPH_2$ (DCPIP reduced by ascorbate). Traces b and c were fitted between 1 and 60 ms with a biexponential function to take into account both the second-order process of Fd reduction and the slow $P700^+$ decay (black traces with fits extrapolated to time 0). The best-fit rates of the fastest component (due to Fd reduction) are k_{obs} = 75 and 151 s^{-1} for b and c, respectively. Assuming pseudo-first order conditions with $k_{obs} = k_{on} \times [Fd]_{free}$ (k_{on} = second-order rate of Fd reduction; $[Fd]_{free}$ = [Fd not bound to PSI] = 0.93 and 1.91 µM from the K_d fit (see Supp. Figure 13), one obtains k_{on} = 8.0 and 7.9 × 10^7 $M^{-1}s^{-1}$ from the independent fits of b and c. On short time scales (t < 20 µs, see orange ellipse), fast-decaying signals due to β-carotene triplet states are present which obscure the signals due to ET. These triplet signals are Fd-independent and are eliminated by subtracting the signal without Fd from those with Fd, as shown in **Part B**. Moreover, the subtraction procedure allows the signals due to PSI charge separation ($P700^+$ $(F_A\ F_B)_{1red}$) to be eliminated so that only Fd reduction by $(F_A\ F_B)_{1red}$ is observed. The difference kinetics are essentially first-order with only a minor contribution due to second-order Fd reduction (see black traces at short times in Part A). The signal increase with [Fd] reflects the binding equilibrium between PSI and Fd with the first-order signal amplitude being proportional to the amount of PSI:Fd complex formed before flash excitation.

Supplementary Figure 13: Titration of Fd binding to PSI.

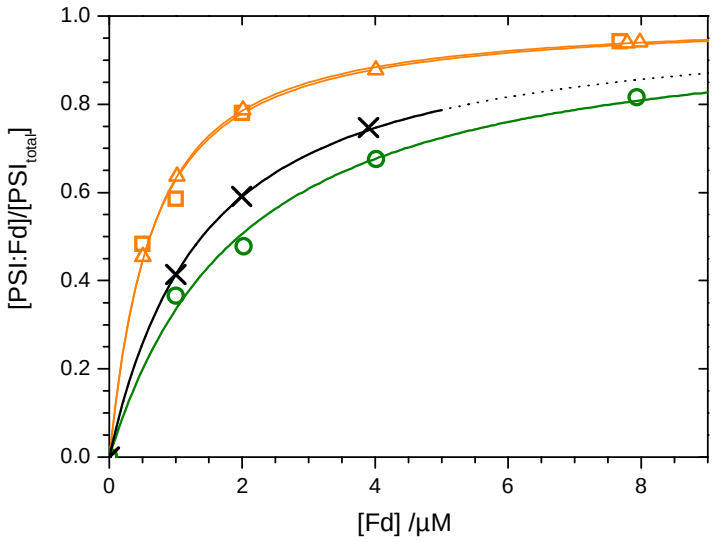

The amplitude of the first-order components of Fd reduction (see Supp. Figure 12 for Fd2, see also single difference kinetics in Figure 7) were plotted as a function of [Fd]. Amplitudes were quantified as the average signal sizes between 0 and 100 µs for Fd1 (orange squares and triangles for 2 different titrations) and Fd1' (black crosses) and between 0 and 400 µs for Fd2 (green circles). The continuous curves were obtained by fitting the data with a simple-binding equilibrium model where the amount of PSI:Fd is solution of a quadratic equation involving the dissociation constant K_d and the concentrations of PSI and Fd. For each Fd, K_d and the asymptotic signal amplitude (100% of PSI binding Fd) were adjustable parameters and the data are plotted as a fraction of the 100% amplitude. K_d values of 0.50, 1.32 and 1.84 µM were determined for Fd1, Fd1' and Fd2, respectively.

Supplementary Figure 14: Kinetics of FNR reduction by $Fd1_{red}$.

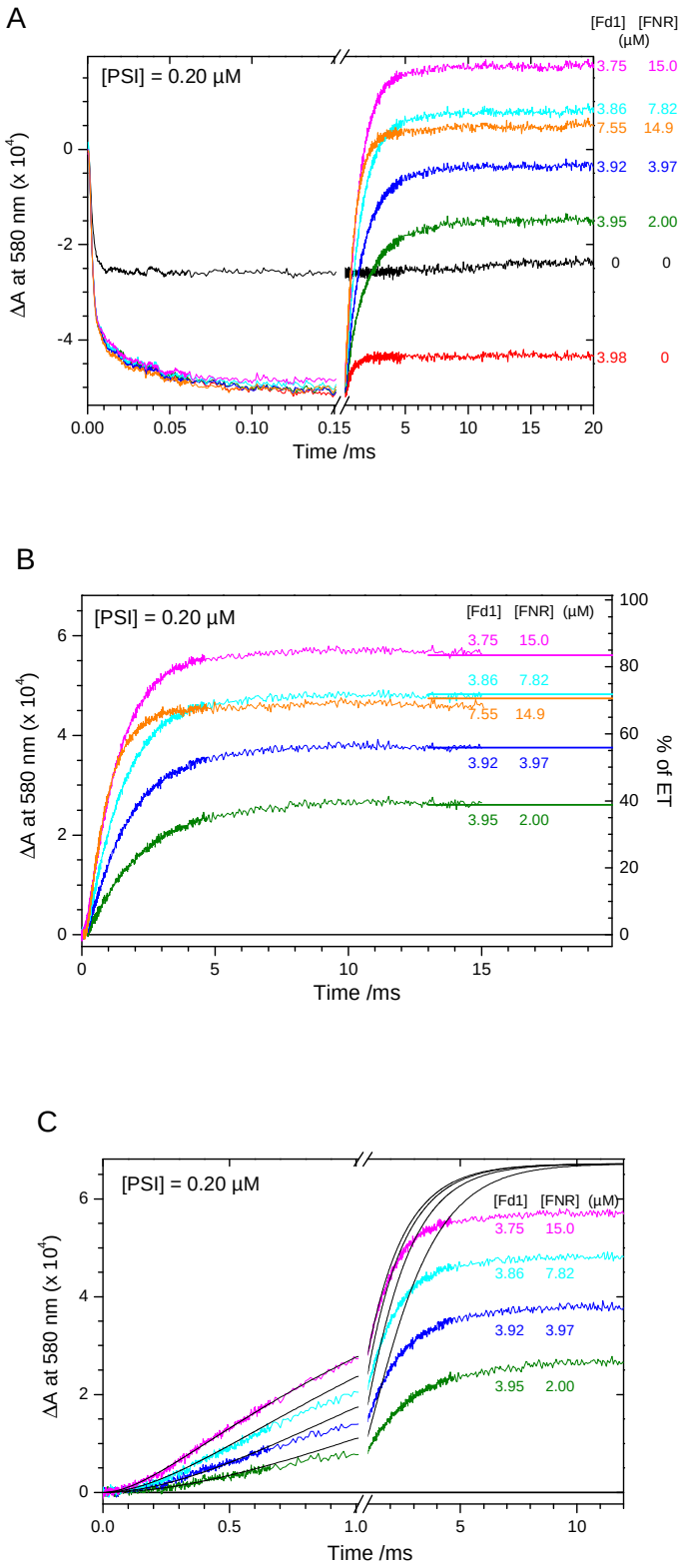

Flash-induced absorption measurements were performed at 580 nm with decreasing [PSI] from 0.209 to 0.197 µM along with Fd1 and FNR additions (or buffer in the reference cuvette). Best-

fits were performed with real PSI concentrations but data in the figure were normalized to 0.2 µM PSI for easier comparison. Concentrations of Fd1 and FNR are indicated for each trace. **Part A** displays raw kinetics. After measurement without addition (black), Fd1 was added first at a concentration of ≈ 4 µM (red), then FNR was added at concentrations increasing from ≈ 2 to 15 µM (green, blue, cyan and magenta) and another Fd1 addition was eventually made (giving ≈ 7.5 µM, orange). Fd reduction leads to a signal decrease which is followed from 0.2 to 3 ms by a small signal increase (red trace). This signal has been investigated in detail [11] and was shown to be due to a non-redox absorption change attributed to an increase in the Fd_{ox} absorption upon binding to PSI. Fd_{ox} binding to PSI occurs after Fd_{red} dissociation, as a diffusion-limited process. Moreover, it occurs similarly whether FNR is present or not and is eliminated when the signal from the reference cuvette (Fd alone) is subtracted from the sample cuvette (Fd + FNR). Addition of FNR induces the appearance of a large positive signal increase following the initial Fd-reduction signal and concomitant with the Fd-binding induced signal. This signal is attributed to the formation of singly-reduced FNR_{sq} in its protonated form ($FADH^{\bullet}$).

Part B displays the differences between the sample and reference cuvettes. The final signal level increases with [FNR] and decreases with the final addition of Fd1. This shows that FNR reduction by Fd_{red} is only partial and the redox equilibrium: $Fd_{red} + FNR_{ox} \leftrightarrow Fd_{ox} + FNR_{sq}$ must be considered. The amplitudes of the final signal levels (between 10 and 15 ms) were fitted using this equilibrium reaction and neglecting the presence Fd:FNR complexes in different redox states. Two adjustable parameters were used, the equilibrium constant $K_{eq} = [Fd_{ox}]\times[FNR_{sq}]/([Fd_{red}]\times[FNR_{ox}])$, and the signal amplitude corresponding to full FNR reduction. With $[Fd_{red}] + [FNR_{sq}] = [PSI]$, the equation giving the ET extent, that is $[FNR_{sq}]/[PSI]$, is a simple quadratic equation. The best-fit parameters are $K_{eq} = 1.26$, ΔA for 100% ET = 6.72×10^{-4} and the resulting best-fit signal levels are shown as horizontal lines. Data can also be read as ET extent using the right vertical scale.

Part C displays kinetics of part A with emphasis on the short time scale. The kinetics between 0 and 0.5 ms were globally fitted using the following kinetic model: $Fd_{red} + FNR_{ox} \rightarrow Fd_{ox}{:}FNR_{sq} \rightarrow Fd_{ox} + FNR_{sq}$. The rates k_{on} and k_{limit} of the two consecutive reactions were taken as adjustable parameters whereas the 100% ET signal was used as a fixed value. From the best fit values ($k_{on} = 4.1 \times 10^{8}$ $M^{-1}s^{-1}$ and $k_{limit} = 640$ s^{-1}), the kinetics were calculated up to completion of the reactions (black traces). The cyan trace ([FNR] = 7.82 µM) and the corresponding calculated kinetics are also shown in Figure 8.

Supplementary Figure 15: Kinetics of NiR reduction by Fd1 and Fd2.

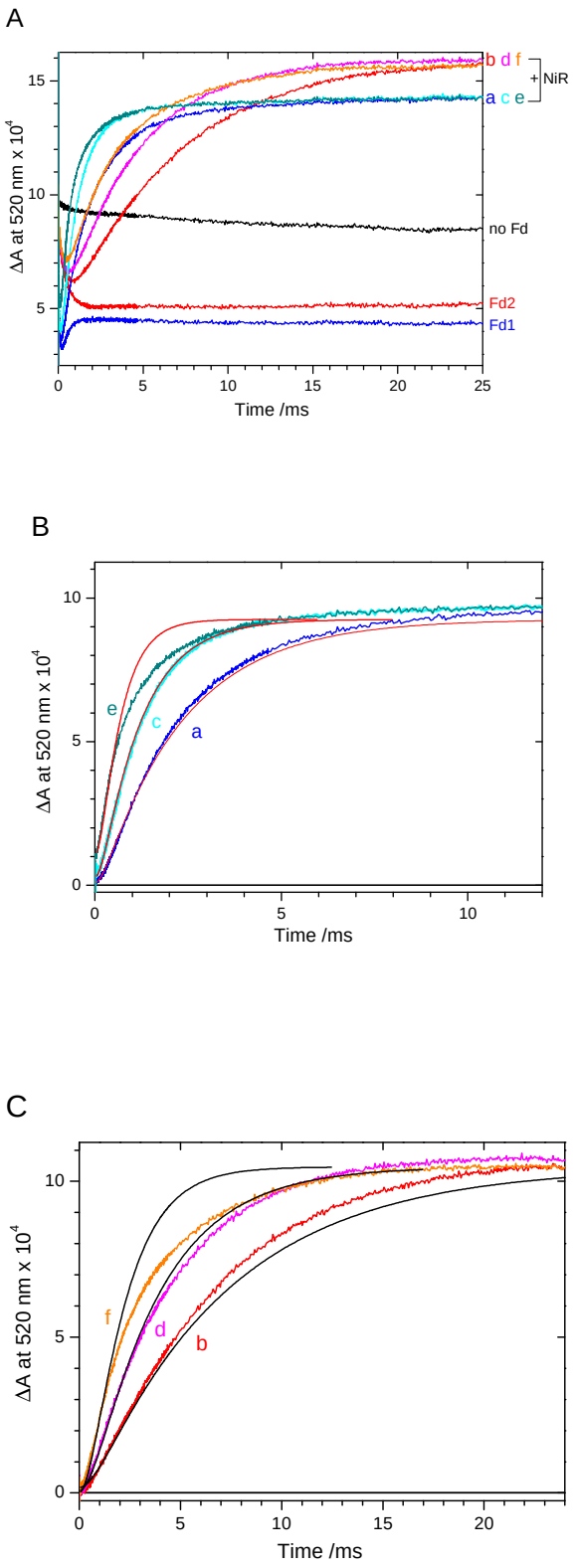

Flash-induced absorption measurements were performed at 520 nm with decreasing [PSI] from 0.243 to 0.231 µM along with Fd1/2 and NiR additions (or buffer in the reference cuvette). All data in the figure were normalized to 0.243 µM µM PSI for easier comparison. **Part A** displays

raw kinetics. In the absence of Fd (trace no Fd), charge separation leads to a positive signal resulting from a major positive contribution due to P700 oxidation and a minor negative contribution due to (F_A F_B) reduction. Addition of either Fd1 (4.79 µM) or Fd2 (4.77 µM) leads to a signal decrease (traces Fd1 and F2). In the case of Fd1, this initial decrease is followed by a smaller increase at t < 2 ms, which results from Fd_{ox} binding to PSI (see Supp. Figure 14A for a similar signal at 580 nm). No such signal is observable with Fd2, although preliminary experiments (not shown) suggest that it may be present at higher [Fd2]. NiR at increasing concentrations was added with both Fds: 3.11 µM for a and b, 6.32 µM for c and d and 12.74 µM for e and f. Traces a, c, e and b, d, f were recorded with Fd1 and Fd2, respectively. **Parts B and C** display the signal differences between the sample cuvettes (Fd + NiR) and the reference cuvettes (Fd) for Fd1 and Fd2, respectively. With each Fd, the final levels are identical for every [NiR], which indicates complete single reduction of NiR, in contrast to what is observed with FNR. These levels are different for Fd1 and Fd2, which also suggests that their respective contributions are different. For each Fd, the kinetics were globally fitted using the following simple kinetic model: $Fd_{red} \rightarrow$ free Fd_{red} + $NiR_{ox} \rightarrow Fd_{ox}$ + NiR_{1red} with rate constants k_{off} and k_{on} for the 2 consecutive reactions. Starting from [Fd_{red}] = [PSI] at t = 0 and within the first-order approximation ([NiR_{ox}] >> [Fd_{red}]), one gets: [NiR_{1red}](t) = [PSI]×[$-k_2\ e^{-koff\ t} + k_{off}\ e^{-k2\ t} + k_2 - k_{off}$]/($k_2$-$k_{off}$) with $k_2 = k_{on} \times$ [NiR_{ox}]. For each Fd, the adjustable parameters were the following: k_{on}, k_{off}, the final signal amplitude, and an offset to take into account the fact that all signals do no start from 0 (very small in all cases except for trace e). The following best-fit parameters were obtained: for Fd1, $k_{on} = 1.43 \times 10^8\ M^{-1}s^{-1}$ and $k_{off} = 5231\ s^{-1}$; for Fd2, $k_{on} = 0.47 \times 10^8\ M^{-1}s^{-1}$ and $k_{off} = 1410\ s^{-1}$. These values are similar to those obtained by single fits of the kinetics in Figure 9. However these global fits are rather poor, especially for the highest [NiR] (traces e and f). In the case of Fd1, this may arise, at least partially, from the fact that some Fd1:NiR complex is formed in darkness, as indicated by the significant initial offset in trace e. Fd1:NiR complex formation should result in a lower amount of PSI:Fd1 through binding competition. In turn, subtraction of the reference cuvette is not perfect as there is more PSI:Fd complex in this cuvette and then, a larger amount of fast Fd reduction than in the sample cuvette, and this is expected to result in the observed offset. In the case of Fd2, there is no significant offset in f, which indicates that the dark amount of Fd2:NiR can be neglected. One (partial) explanation for the bad fit of trace f could be that Fd2 reduction should be explicitly taken into account in the kinetic model, as it is not that fast compared to the following processes of Fd_{red} dissociation and NiR reduction. It was not checked further by numerical simulations of the kinetics that the above explanations for the poor global fits are correct, as the main

conclusion of this study, which is that NiR reduction by Fd1 is about 3-times faster than by Fd2, is approximately valid for the 3 tested [NiR].

Supplementary Figure 16: Phylogenetic analysis of photosynthetic-type Fds from cyanobacteria.

Part A: Phylogenetic unrooted tree of all photosynthetic-type [2Fe-2S] Fds from 83 different cyanobacterial strains and from maize, *Arabidopsis thaliana* and *Chlamydomonas reinhardtii*. Sequence alignment was performed with MUSCLE and tree construction was done with the neighbor-joining method, both methods being provided in the SeaView integrated software. Bootstrap values (from 0 to 100) were obtained from 1000 repetitions. The branches and leaves are colored according to the value of the X:Y doublet: blue for Val:Phe, Phe:Phe, Ile:Phe, Ile:Ile and Thr:Phe; red for Ser:Phe; green and dashed light green for Thr:Gly. Values of X:Y are indicated at the end of the labels. Labels of eucaryotic Fds are colored green. The dashed light green branch correspond to Fds with a large C-terminal extension. It includes Fed2 from *Synechocystis* 6803, Fd3 from *T. elongatus*, FdC2 from *Arabidopsis thaliana* and Fdx6 from *Chlamydomonas reinhardtii*.

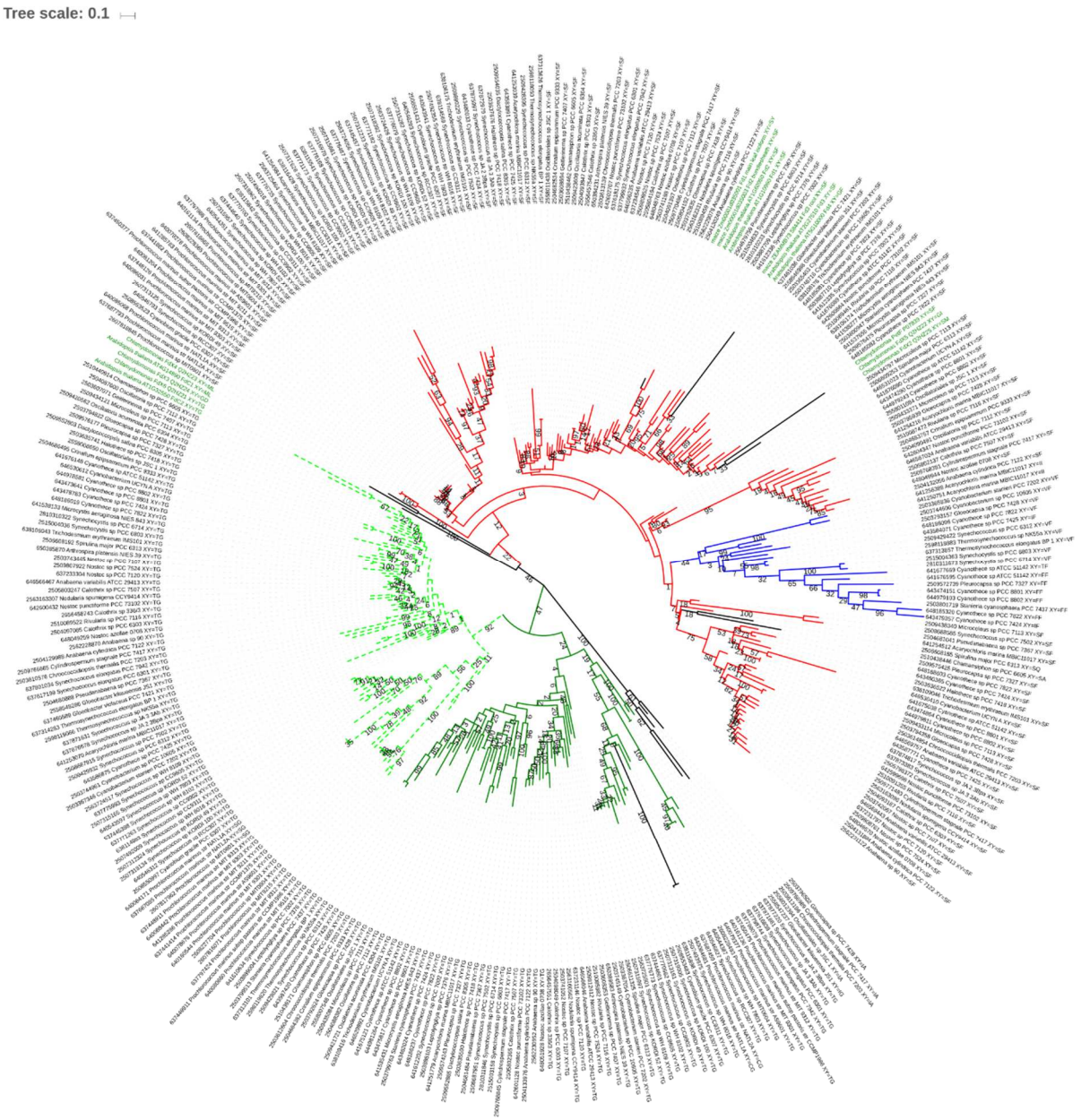
Tree scale: 0.1

Part B: Sequence alignment which was used for building the phylogenetic tree of Figure 10. The sequences are grouped by cyanobacterial strain. All strains have at least one “red” Fd, have one “light green” Fd (with a C-terminal extension) and all except one (*Synechococcus* sp. PCC 7002) have one “green” Fd . The cluster-liganding Cys are shown on a yellow background whereas the residues X and Y are on a cyan background.

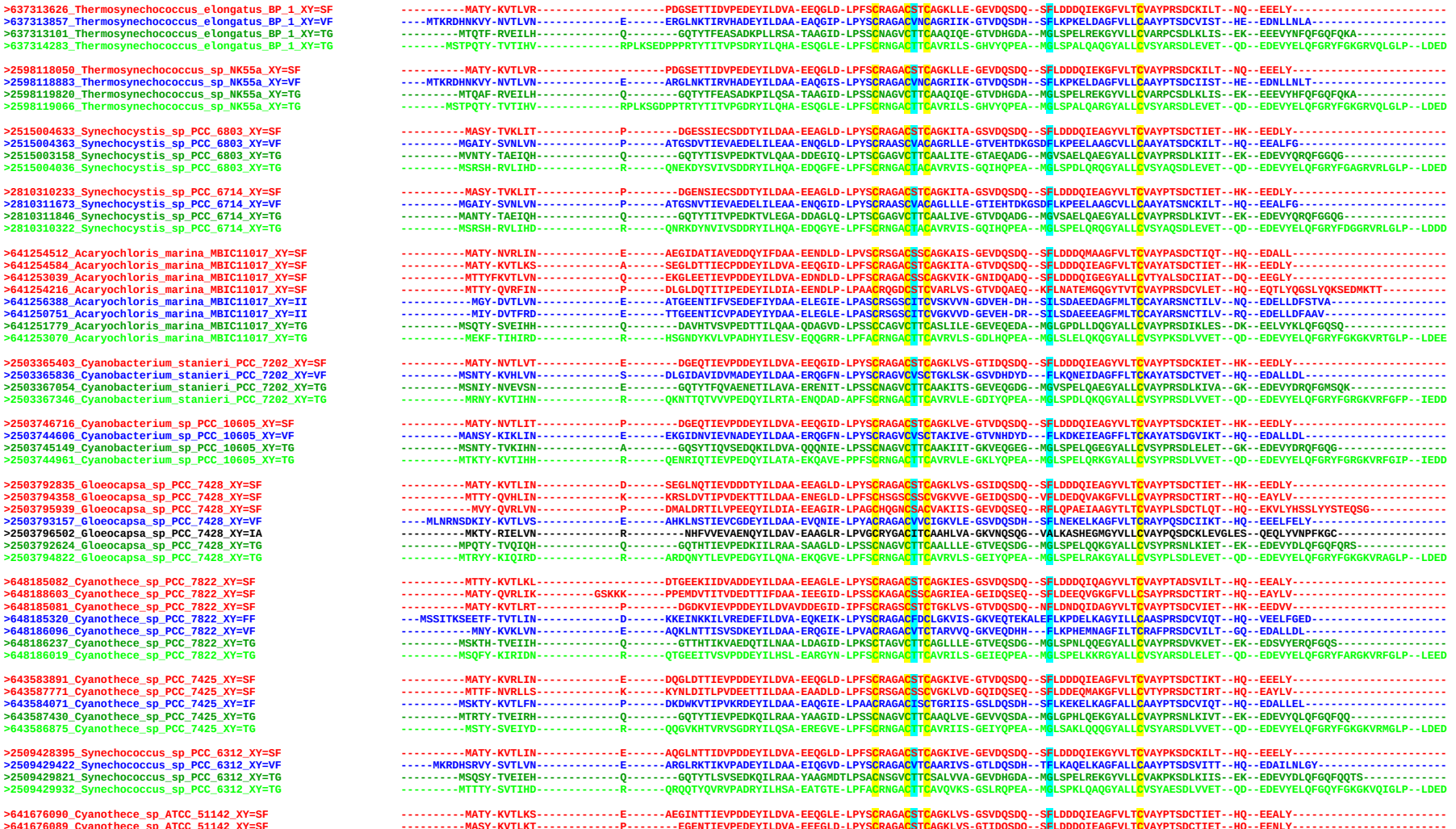

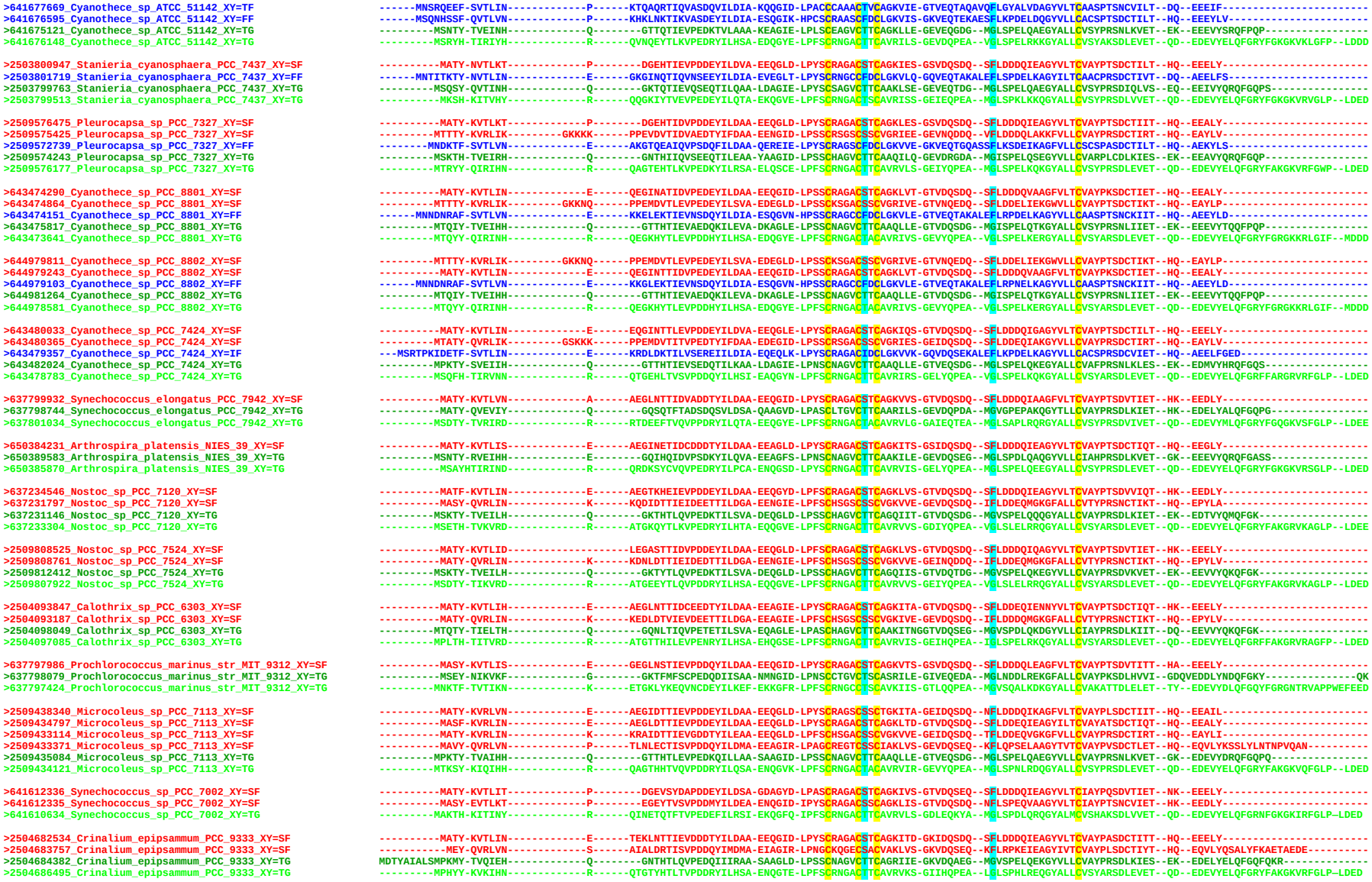
>641677669_Cyanothece_sp_ATCC_51142_XY=TF
>641676595_Cyanothece_sp_ATCC_51142_XY=FF
>641675121_Cyanothece_sp_ATCC_51142_XY=TG
>641676148_Cyanothece_sp_ATCC_51142_XY=TG
>2503800947_Stanieria_cyanosphaera_PCC_7437_XY=SF
>2503801719_Stanieria_cyanosphaera_PCC_7437_XY=FF
>2503799763_Stanieria_cyanosphaera_PCC_7437_XY=TG
>2503799513_Stanieria_cyanosphaera_PCC_7437_XY=TG
>2509576475_Pleurocapsa_sp_PCC_7327_XY=SF
>2509575425_Pleurocapsa_sp_PCC_7327_XY=SF
>2509572739_Pleurocapsa_sp_PCC_7327_XY=FF
>2509574243_Pleurocapsa_sp_PCC_7327_XY=TG
>2509576177_Pleurocapsa_sp_PCC_7327_XY=TG
>643474290_Cyanothece_sp_PCC_8801_XY=SF
>643474864_Cyanothece_sp_PCC_8801_XY=SF
>643474151_Cyanothece_sp_PCC_8801_XY=FF
>643475817_Cyanothece_sp_PCC_8801_XY=TG
>643473641_Cyanothece_sp_PCC_8801_XY=TG
>644979811_Cyanothece_sp_PCC_8802_XY=SF
>644979243_Cyanothece_sp_PCC_8802_XY=SF
>644979103_Cyanothece_sp_PCC_8802_XY=FF
>644981264_Cyanothece_sp_PCC_8802_XY=TG
>644978581_Cyanothece_sp_PCC_8802_XY=TG
>643480033_Cyanothece_sp_PCC_7424_XY=SF
>643480365_Cyanothece_sp_PCC_7424_XY=SF
>643479357_Cyanothece_sp_PCC_7424_XY=IF
>643482024_Cyanothece_sp_PCC_7424_XY=TG
>643478783_Cyanothece_sp_PCC_7424_XY=TG
>637799932_Synechococcus_elongatus_PCC_7942_XY=SF
>637798744_Synechococcus_elongatus_PCC_7942_XY=TG
>637801034_Synechococcus_elongatus_PCC_7942_XY=TG
>650384231_Arthrospira_platensis_NIES_39_XY=SF
>650389583_Arthrospira_platensis_NIES_39_XY=TG
>650385870_Arthrospira_platensis_NIES_39_XY=TG
>637234546_Nostoc_sp_PCC_7120_XY=SF
>637231797_Nostoc_sp_PCC_7120_XY=SF
>637231146_Nostoc_sp_PCC_7120_XY=TG
>637233304_Nostoc_sp_PCC_7120_XY=TG
>2509808525_Nostoc_sp_PCC_7524_XY=SF
>2509808761_Nostoc_sp_PCC_7524_XY=SF
>2509812412_Nostoc_sp_PCC_7524_XY=TG
>2509807922_Nostoc_sp_PCC_7524_XY=TG
>2504093847_Calothrix_sp_PCC_6303_XY=SF
>2504093187_Calothrix_sp_PCC_6303_XY=SF
>2504098049_Calothrix_sp_PCC_6303_XY=TG
>2504097085_Calothrix_sp_PCC_6303_XY=TG
>637797986_Prochlorococcus_marinus_str_MIT_9312_XY=SF
>637798079_Prochlorococcus_marinus_str_MIT_9312_XY=TG
>637797424_Prochlorococcus_marinus_str_MIT_9312_XY=TG
>2509438340_Microcoleus_sp_PCC_7113_XY=SF
>2509434797_Microcoleus_sp_PCC_7113_XY=SF
>2509433114_Microcoleus_sp_PCC_7113_XY=SF
>2509433371_Microcoleus_sp_PCC_7113_XY=SF
>2509435084_Microcoleus_sp_PCC_7113_XY=TG
>2509434121_Microcoleus_sp_PCC_7113_XY=TG
>641612336_Synechococcus_sp_PCC_7002_XY=SF
>641612335_Synechococcus_sp_PCC_7002_XY=SF
>641610634_Synechococcus_sp_PCC_7002_XY=TG
>2504682534_Crinalium_epipsammum_PCC_9333_XY=SF
>2504683757_Crinalium_epipsammum_PCC_9333_XY=SF
>2504684382_Crinalium_epipsammum_PCC_9333_XY=TG
>2504686495_Crinalium_epipsammum_PCC_9333_XY=TG

Part C: Cyanobacteria having one (or two) Fds from the blue group are marked in blue in the phylogenetic tree of cyanobacteria published by Shih et al. [12].

Supplementary Figure 17A: Superimposition of Fd2 to the structure of the PSI:Fd1 complex Fd2 was aligned to Fd1 in the PSI:Fd co-crystal structure (PDB: 5ZF0) by using the α-carbons. The PSI subunits in proximity to Fd2 are shown in cartoon mode: PsaA, C, D, E are colored grey, light pink, cyan (transparent) and yellow, respectively. Fd2 is shown in green. The Fd2 cluster, F_B and F_A are visible from left to right.

After alignment, PSI atoms within a distance of 2 Å from Fd are identified as belonging to Arg36 and Arg40 from PsaA and Lys34 from PsaC. These residues, colored by element, are displayed as sticks together with the Fd2 residues involved in steric hindrance (as well as Phe72). The pairs of residues involved in steric hindrance are labeled **a** ($Arg40_{PsaA}$, $Asp69_{Fd2}$), **b** ($Arg36_{PsaA}$, $Asp79_{Fd2}$) and **c** ($Lys34_{PsaC}$, $Tyr46_{Fd2}$). Whereas a very strong steric clash is involved in **a**, only a limited steric hindrance is involved in **b** and **c**.

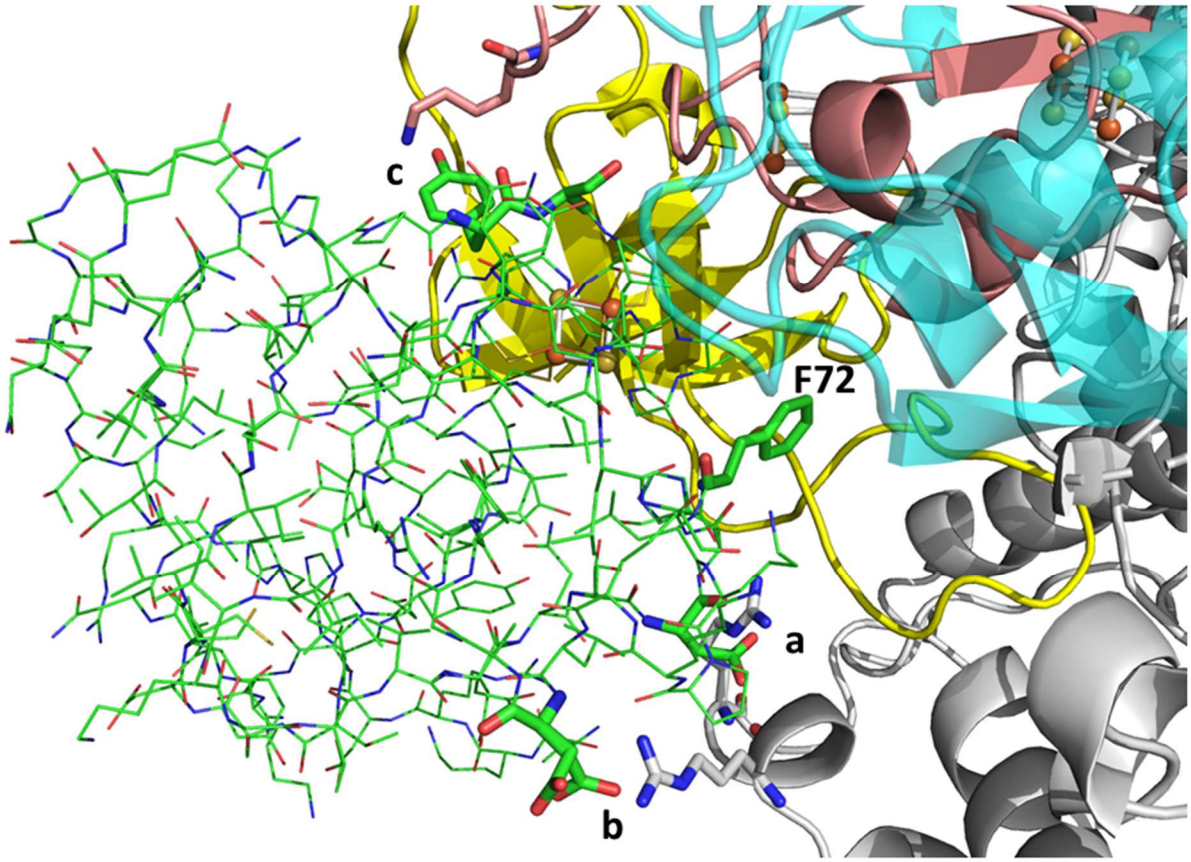

Supp. Figure 17B: Discussion related to intracomplex reduction of Fds by PSI

It was initially proposed that the presence of several phases in the kinetics of intracomplex Fd reduction was due to different conformations of the PSI:Fd complex [13], leading to different ET electronic couplings (conformational model). More recently, an alternative explanation was proposed where only the fastest sub-µs phase corresponds to real ET [11], in the sense of a non-adiabatic tunneling reaction [14, 15]. In this interpretation, intracomplex Fd reduction is incomplete during the initial sub-µs phase due to a small equilibrium constant K_{ET} of the reaction: $PSI_{red}:Fd_{ox} \rightarrow PSI_{ox}:Fd_{red}$. Then, further Fd reduction proceeds due to energetic relaxation of the $PSI_{ox}:Fd_{red}$ and/or fast dissociation of Fd_{red} from PSI (relaxation model). In this context, it must be recalled that there is some uncertainty about the midpoint potential of (F_A F_B) with published values which span between -440 and -550 mV [16-18]. Moreover, it has been recently found that the driving force for Fd reduction within the complex is lower than what can be calculated from the midpoint potentials of the separated partners [11], a situation which may favor a fast turnover of Fd reduction and release.

Within this model, the difference in the intracomplex kinetics of Fd reduction should mostly depend upon the driving force of Fd reduction (assuming similar distances and ET couplings with the different Fds). Indeed the higher midpoint potential of Fd1' (*vs* Fd1) would correspond to a higher value of K_{ET} and consequently a larger contribution of the sub-µs phase. The slow Fd2 kinetics would also be attributed to the fact that the Fd2 intracomplex reduction is endergonic with a very low value of K_{ET} and consequently no significant sub-µs phase.

Supp. **Table 1.** Data collection and structural refinement statistics of Fd crystals.

Data collection	Fd2 (Native)	Fd1(Native)
Beamline	BL38XU (SPring-8)	BL41XU (SPring-8)
Wavelength (Å)	1.000	1.000
Average dose (MGy)	0.22	0.67
Space group	$P2_1$	$C2$
Unit cell	a = 27.95 Å b = 51.12 Å c = 31.57 Å α = γ = 90.00°, β = 116.15°	a = 56.17 Å b = 53.22 Å c = 32.29 Å α = γ = 90.00°, β = 92.67°
Resolution (Å)	28.34-1.38 (1.47-1.38) [b]	38.61-1.55 (1.64-1.55) [b]
Unique reflections	16,325 (2,593)	13,408 (1,983)
Redundancy	3.68 (3.62)	3.30 (2.95)
Completeness	99.3 (98.9)	96.5 (90.1)
R_{merge} [c]	5.6 (58.5)	6.4 (38.3)
I/σ(I)	12.82 (2.00)	12.04 (2.90)
R-means [d] (%)	6.6 (68.8)	7.6 (46.8)
CC(1/2) [e]	99.9 (71.8)	99.7 (86.6)
Structural refinement		
R_{factor}	0.1124	0.1327
R_{free}	0.1570	0.1759
Number of atoms		
Proteins	887	842
Ligands	9	27
Water	109	96
Number of residues	107	97
R.m.s.d. (bond)	0.0213	0.0111
R.m.s.d. (angle)	2.0860	1.4082
Mean B-factor	18.168	14.938
Ramachandran plot [f]		
Favored (%)	96.19	96.84
Allowed (%)	3.81	3.16
Outliers (%)	0.00	0.00

[a] Average diffraction weighted dose calculated by RADDOSE-3D [19].

[b] Statistics for the highest resolution shell are shown in parentheses.

[c] $R_{merge} = \sum_{hkl} \sum_i |I_i(hkl) - \langle I(hkl) \rangle| / \sum_{hkl} \sum_i I_i\,(hkl)$

where $I_i(hkl)$ is the intensity of the reflection and $\langle I(hkl) \rangle$ is the mean intensity of a group of equivalent reflection.

[d] *R*-factor independent of the redundancy.

[e] Percentage of correlation between intensities from two random half-datasets.

[f] Calculated with the MolProbity [20].

Supp. Table 2. Dipole moments characteristics of Fd2, Fd1 and orthologues of Fd1 in six other cyanobacteria, including FdN, and of the heterocyst Fd from *Nostoc* PCC7120.

Cyanobacterial strain	μ_{Fdox} (Debyes)	μ_{Fdred} (Debyes)	Angle (μ_{Fdox}, μ_{Fdred}) (degrees)	Total charge (Fd_{ox})
T. elongatus Fd2 (tlr1236)	378	422	4.4	-6
T. elongatus Fd1 (tsl1009)	186	234	6.5	-17
Nostoc. 7119 FdN (all4148)	285	334	3.3	-18
Syn. 6803 (ssl0020)	247	291	5.9	-18
Leptolyngbya boryana	239	292	0.6	-18
Mastigocladus laminosus	370	408	5.1	-15
Aphanothece sacrum	328	379	1.1	-15
Arthrospira platensis	234	279	5.4	-19
All strains Fd1	270 ± 62	316 ± 61	4 ± 2.4	-17.1 ± 1.6
Nostoc. 7120 heterocyst Fd (all1430)	453	481	5.6	-13

The following structures were used for the calculations: PDB 5AUI for *T. elongatus* Fd1 [2], PDB 1OFF for *Syn*. 6803 [21], PDB 1QT9 for *Nostoc* 7119 FdN [22], PDB 3B2G for *Leptolyngbya boryana* [23], PDB 4FXC for *Arthrospira platensis* [24], PDB 3AV8 for *Aphanothece sacrum* [25], PDB 1RFK for *Mastigocladus laminosus* [26], PDB 1FRD for *Nostoc* 7120 heterocyst Fd [27].

References.

1. Kabsch W: **A solution for the best rotation to relate two sets of vectors**. *Acta Crystallographica Section A: Crystal Physics, Diffraction, Theoretical and General Crystallography* 1976, **32**(5):922-923.
2. Mutoh R, Muraki N, Shinmura K, Kubota-Kawai H, Lee YH, Nowaczyk MM, Rogner M, Hase T, Ikegami T, Kurisu G: **X-ray Structure and Nuclear Magnetic Resonance Analysis of the Interaction Sites of the Ga-Substituted Cyanobacterial Ferredoxin**. *Biochemistry* 2015, **54**(39):6052-6061.
3. Rypniewski WR, Breiter DR, Benning MM, Wesenberg G, Oh BH, Markley JL, Rayment I, Holden HM: **Crystallization and Structure Determination to 2.5-a Resolution of the Oxidized [Fe2-S2] Ferredoxin Isolated from Anabaena-7120**. *Biochemistry* 1991, **30**(17):4126-4131.
4. Venyaminov SY, Kalnin NN: **Quantitative Ir Spectrophotometry of Peptide Compounds in Water (H2o) Solutions .2. Amide Absorption-Bands of Polypeptides and Fibrous Proteins in Alpha-Coil, Beta-Coil, and Random Coil Conformations**. *Biopolymers* 1990, **30**(13-14):1259-1271.
5. Chirgadze YN, Shestopalov BV, Venyaminov SY: **Intensities and Other Spectral Parameters of Infrared Amide Bands of Polypeptides in Beta- and Random Forms**. *Biopolymers* 1973, **12**(6):1337-1351.
6. Venyaminov SY, Kalnin NN: **Quantitative Ir Spectrophotometry of Peptide Compounds in Water (H2o) Solutions .1. Spectral Parameters of Amino-Acid Residue Absorption-Bands**. *Biopolymers* 1990, **30**(13-14):1243-1257.
7. Hienerwadel R, Boussac A, Breton J, Diner BA, Berthomieu C: **Fourier transform infrared difference spectroscopy of photosystem II tyrosine D using site-directed mutagenesis and specific isotope labeling**. *Biochemistry* 1997, **36**(48):14712-14723.
8. Susi H, Byler DM, Gerasimowicz WV: **Vibrational Analysis of Amino-Acids - Cysteine, Serine, Beta-Chloroalanine**. *J Mol Struct* 1983, **102**(1-2):63-79.
9. Barth A: **The infrared absorption of amino acid side chains**. *Prog Biophys Mol Bio* 2000, **74**(3-5):141-173.
10. Emsley P, Lohkamp B, Scott WG, Cowtan K: **Features and development of Coot**. *Acta Crystallogr D* 2010, **66**:486-501.
11. Setif P, Mutoh R, Kurisu G: **Dynamics and energetics of cyanobacterial photosystem I:ferredoxin complexes in different redox states**. *Bba-Bioenergetics* 2017, **1858**(7):483-496.
12. Shih PM, Wu DY, Latifi A, Axen SD, Fewer DP, Talla E, Calteau A, Cai F, de Marsac NT, Rippka R *et al*: **Improving the coverage of the cyanobacterial phylum using diversity-driven genome sequencing**. *P Natl Acad Sci USA* 2013, **110**(3):1053-1058.
13. Setif PQY, Bottin H: **Laser Flash Absorption-Spectroscopy Study of Ferredoxin Reduction by Photosystem-I - Spectral and Kinetic Evidence for the Existence of Several Photosystem-I Ferredoxin Complexes**. *Biochemistry* 1995, **34**(28):9059-9070.
14. Marcus RA, Sutin N: **Electron Transfers in Chemistry and Biology**. *Biochimica et biophysica acta* 1985, **811**(3):265-322.
15. Moser CC, Keske JM, Warncke K, Farid RS, Dutton PL: **Nature of Biological Electron-Transfer**. *Nature* 1992, **355**(6363):796-802.
16. Brettel K, Leibl W: **Electron transfer in photosystem I**. *Bba-Bioenergetics* 2001, **1507**(1-3):100-114.
17. Heathcote P, Williamssmith DL, Sihra CK, Evans MCW: **Role of Membrane-Bound Iron-Sulfur Centers-a and Centers-B in Photosystem-I Reaction Center of Spinach-Chloroplasts**. *Biochimica et biophysica acta* 1978, **503**(2):333-342.
18. Jordan R, Nessau U, Schlodder E: **Charge recombination between the reduced iron-sulphur clusters and P700**. *Photosynthesis: Mechanisms and Effects, Vols I-V* 1998:663-666.

19. Zeldin OB, Gerstel M, Garman EF: **RADDOSE-3D: time- and space-resolved modelling of dose in macromolecular crystallography**. *J Appl Crystallogr* 2013, **46**:1225-1230.
20. Chen VB, Arendall WB, Headd JJ, Keedy DA, Immormino RM, Kapral GJ, Murray LW, Richardson JS, Richardson DC: **MolProbity: all-atom structure validation for macromolecular crystallography**. *Acta Crystallogr D* 2010, **66**:12-21.
21. van den Heuvel RHH, Svergun DI, Petoukhov MV, Coda A, Curti B, Ravasio S, Vanoni MA, Mattevi A: **The active conformation of glutamate synthase and its binding to ferredoxin**. *J Mol Biol* 2003, **330**(1):113-128.
22. Morales R, Chron MH, Hudry-Clergeon G, Petillot Y, Norager S, Medina M, Frey M: **Refined X-ray structures of the oxidized, at 1.3 angstrom, and reduced, at 1.17 angstrom, [2Fe-2S] ferredoxin from the cyanobacterium Anabaena PCC7119 show redox-linked conformational changes**. *Biochemistry* 1999, **38**(48):15764-15773.
23. Sakakibara Y, Kimura H, Iwamura A, Saitoh T, Ikegami T, Kurisu G, Hase T: **A new structural insight into differential interaction of cyanobacterial and plant ferredoxins with nitrite reductase as revealed by NMR and X-ray crystallographic studies**. *J Biochem-Tokyo* 2012, **151**(5):483-492.
24. Fukuyama K, Ueki N, Nakamura H, Tsukihara T, Matsubara H: **Tertiary Structure of [2fe-2s] Ferredoxin from Spirulina-Platensis Refined at 2.5 Angstrom Resolution - Structural Comparisons of Plant-Type Ferredoxins and an Electrostatic Potential Analysis**. *J Biochem-Tokyo* 1995, **117**(5):1017-1023.
25. Kameda H, Hirabayashi K, Wada K, Fukuyama K: **Mapping of Protein-Protein Interaction Sites in the Plant-Type [2Fe-2S] Ferredoxin**. *Plos One* 2011, **6**(7).
26. Fish A, Danieli T, Ohad I, Nechushtai R, Livnah O: **Structural basis for the thermostability of ferredoxin from the cyanobacterium Mastigrocladus laminosus**. *J Mol Biol* 2005, **350**(3):599-608.
27. Jacobson BL, Chae YK, Markley JL, Rayment I, Holden HM: **Molecular-Structure of the Oxidized, Recombinant, Heterocyst [2fe-2s] Ferredoxin from Anabaena-7120 Determined to 1.7-Angstrom Resolution**. *Biochemistry* 1993, **32**(26):6788-6793.